

3020



**INVESTIGATIONS OF THIN FILMS OF METALS AND
METAL OXIDES DEPOSITED BY NEBULIZED SPRAY
PYROLYSIS**

**A REPORT SUBMITTED IN PARTIAL FULFILLMENT OF THE
REQUIREMENT OF THE DEGREE OF MASTER OF SCIENCE AS A PART OF
INTEGRATED Ph. D. PROGRAMME**

BY

SACHIN PARASHAR



TO

MANIPAL ACADEMY OF HIGHER EDUCATION

THROUGH

JAWAHARLAL NEHRU CENTRE FOR ADVANCED SCIENTIFIC RESEARCH

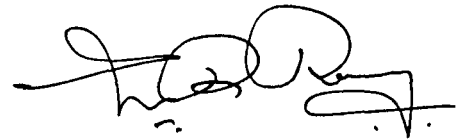
BANGALORE, INDIA

FEBRUARY 1999

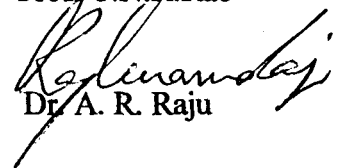
530.4175
N99

STATEMENT

Certified that the work described here has been done under my supervision at Jawaharlal
Nehru Centre for Advanced Scientific Research, Jakkur, Bangalore, INDIA.



Prof. C.N.R. Rao



Dr. A. R. Raju

CONTENTS

STATEMENT

ACKNOWLEDGEMENTS

SUMMARY

1. THIN FILM DEPOSITION TECHNIQUES.....	1
1.1 Physical vapor deposition.....	1
1.2 Chemical vapor deposition.....	6
2. SCOPE OF THE PRESENT INVESTIGATION.....	12
3. EXPERIMENTAL.....	16
3.1 Nebulized spray pyrolysis.....	16
3.2 Copper films.....	22
3.3 Cobalt and granular copper-cobalt alloy films.....	24
3.4 Films of charge-ordered rare earth manganates.....	24
4. RESULTS AND DISCUSSION.....	26
4.1 Copper films.....	26
4.2 Cobalt and granular copper-cobalt alloy films.....	41
4.3 Films of charge-ordered rare earth manganates.....	48
5. REFERENCES.....	66

ACKNOWLEDGMENTS

I wish to express my sincere gratitude to Prof. C.N.R.Rao, FRS for suggesting the problems, invaluable guidance and moral support which has been instrumental in shaping me as a research student. I am sure that I will continue to receive the same forever. He has taught me how to work professionally and to present it in the best manner.

I am extremely thankful to my co-guide Dr.A.R.Raju who was there with me in carrying out the experiments. His systematic way of working and excellent knowledge about instrumentation has made it possible for me to complete so much work in such short span of time.

I am thankful to all the professors of Chemical Sciences Division, IISc for the courses offered, their help, suggestions and constant encouragement. In particular, I would like to express my sincere gratitude to Prof. S.Chandrasekharan, Prof. J.Chandrasekhar, Prof. T.N.Guru Row, Prof. S.B.Kruphanidhi and Dr. G.Mohan Rao for their help.

I would like to thank Prof. V.Krishnan and Dr. W.H.Madhusudan for day to day help. Mr. Nagaraja Rao and his administration, especially Ms. G. Sukanya had been extremely helpful to me.

I am thankful to Dr. Hemantkumar N. Aiyer with whom I collaborated in my first problem. Dr. V.Ponnambalam taught me a lot of physics for which I am grateful. I sincerely thank my integrated Ph.D. batch-mates Abhijit, Sameer, Smitha, Joy, Subrutho, Navedh, Supriya, Nupur, Urvashi, Moshmi, Vinaya and Jayant. Thanks to my lab mates Messers Murugavel and Sudheendra for their help and patience. Thanks to Anupama, Neeraj, Gopalan, John, Vaidi, Vijay, Gargi, Sujay, Pattu, Alagiri and C P Vinod for the support when I was depressed. Thanks to M. K. Renganathan, Anil, Vasu and Srinath for their assistance in my work. I also thank Dr. Govindraj for his help at IISc.

I specially thank Dr. S.K.Jain for his motivating me to study chemistry.

I specially thank Prof. K.V.Sane for giving me first opportunity to work in his research laboratory in University of Delhi.

My father has been the most important person in my life and has provided me every comfort from credit cards to air tickets and has stood by me despite all the problems. Mummy and Golu are all always with me. To all my relatives I am always thankful.

INVESTIGATIONS OF THIN FILMS OF METALS AND METAL OXIDES DEPOSITED BY NEBULIZED SPRAY PYROLYSIS

SUMMARY

Nebulized spray pyrolysis has been employed to deposit metal and metal oxide films on different solid substrates. The following are the important materials investigated in the present study: copper, cobalt, granular copper-cobalt alloys and charge ordered rare earth manganates.

Metallic copper films have been deposited on Si(100) substrates by nebulized spray pyrolysis of $\text{Cu}(\text{acac})_2$, $\text{Cu}(\text{hfac})_2$ and $\text{Cu}(\text{dpm})_2$. The structure and morphology of the films have been examined by X-ray diffraction and scanning electron microscopy. The films are polycrystalline in nature with a preferred (111) orientation. Based on the electrical resistivity data, various transport parameters of the films have been estimated. Growth kinetics and the environmental stability of the films from the precursors have been compared. Taking all the factors into account, $\text{Cu}(\text{dpm})_2$ seems to yield the best films of copper metal.

Thin films of cobalt were deposited on solid substrate by nebulized spray pyrolysis using $\text{Co}(\text{acac})_2$ precursor in hydrogen atmosphere. The films show excellent magnetic and metallic properties. Granular Cu-Co alloy films of the composition $\text{Cu}_{82}\text{Co}_{18}$ and $\text{Cu}_{50}\text{Co}_{50}$ have been obtained by the nebulized spray pyrolysis of mixtures of $\text{Co}(\text{acac})_2$ and $\text{Cu}(\text{acac})_2$ in hydrogen atmosphere. These films show good magnetoresistance at room temperature.

Thin films of charge-ordered $\text{Nd}_{0.5}\text{Ca}_{0.5}\text{MnO}_3$, $\text{Y}_{0.5}\text{Ca}_{0.5}\text{MnO}_3$ and $\text{Nd}_{0.5}\text{Sr}_{0.5}\text{MnO}_3$ have been prepared on Si(100) and $\text{LaAlO}_3(100)$ substrates by the nebulized spray pyrolysis of organometallic precursors. Small electric fields induce insulator-metal transitions in the films with the resistivity decreasing with increasing current. The I-V characteristics are non-ohmic and show some hysteresis. The current-induced negative differential resistance found in these manganate films could have potential technological applications.

* Papers based on work described here have appeared in J. Phys. D: Appl. Phys., (1999) Appl. Phys. Lett., (1999). One paper has been accepted in Mat. Chem. & Phys

INVESTIGATIONS OF THIN FILMS OF METALS AND METAL OXIDES DEPOSITED BY NEBULIZED SPRAY PYROLYSIS

1. THIN FILM DEPOSITION TECHNIQUES

Thin films are few layers of a material supported by a substrate. It has its dimensions in the macroscopic scale along its length and breadth¹⁻³. Its thickness is negligibly small, usually of the order of a few angstroms to few microns. It is also called a two dimensional solid. This two-dimensional nature make it altogether different from its bulk component and it is possible to make films with tailor made properties.

The synthesis of films is the most important matter in this area. Due to the needs to upgrade present day technology, the synthesis of multicomponent/multilayered films of superconductors, semiconductors, metallic granular alloys, insulators and manganates has gained importance. The development of film deposition techniques and the achievement of a good understanding of the basic physical, chemical and materials related processes involved in the synthesis of these films are critical for the successful evolution of this highly interdisciplinary field of research^{4,5}. There are basically two approaches by which thin films can be deposited:

1. Physical vapor deposition (PVD)
2. Chemical vapor deposition (CVD)

1.1. Physical vapor deposition (PVD)

This method basically involves a physical transportation of the required material, by means of a physical method. There are many different techniques that come under this category.

a) *Vacuum Evaporation* - This is the oldest technique of depositing thin films.

Evaporation is done in a vacuum of ($\sim 10^{-3}$ - 10^{-5} torr) by means of a resistive heater, RF heating coil or an electron beam. Depending upon the needs and resources any

one of the evaporation sources can be used. Most common of all these methods is the resistive heater evaporation. Single component films like that of the metals e.g. copper, aluminum etc can be easily deposited. Alloys of metals have also been deposited. Fig.1.1 shows a typical resistive evaporation apparatus.

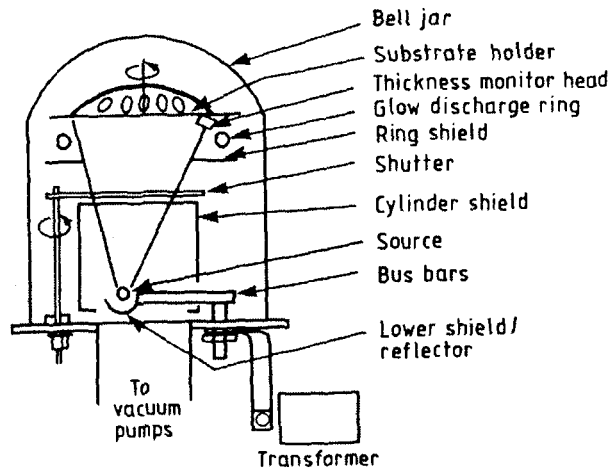


Fig.1.1. Schematic diagram of thermal evaporation unit for making thin films

b) **Sputtering** - It is one of the most commonly used methods of depositing thin films. The principle behind this method is to knock off atoms of the material to be deposited by high-energy bombardment. These high-energy particles are generated with the help

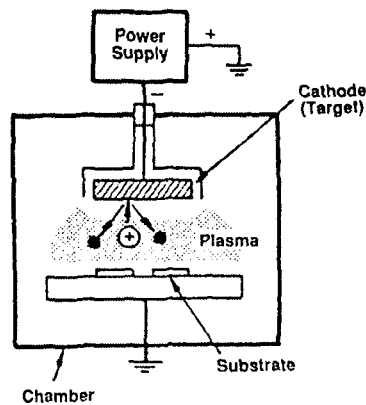


Fig.1.2. Schematic diagram of sputtering unit to deposit thin films

of plasmas. Depending on the needs of material to be deposited, a variety of sputtering techniques have been developed. Fig.1.2. shows the most common sputtering apparatus.

There are many methods in sputtering technique and are described below:

i) DC-Glow Discharge Sputtering - This is the simplest of all the techniques of sputtering and can only be used to make conducting films. The target is cathode here and the substrate is grounded or can be positively biased. In order to get plasma an inert gas (argon or nitrogen) is used. As soon as the negative bias is applied to the target there is an electron emission. As these electrons hit the gas atoms, there is momentum transfer leading to generation of high-energy gas atoms and ions. These high energy gas atoms and ions hit back the target and knock off atoms, of the target material which go and sit on the substrate and forms a film. A continuous emission of electrons is needed from the target for this technique, so conducting samples can only be deposited. In case of non-conducting samples there will be a charging and the glow will last for few seconds only, i.e. only after initialization and stops the film deposition process.

ii) RF sputtering - This was the first improvement over the dc sputtering. Here instead of a DC power source, a RF source is used which works at 13.56 MHz. Due to the presence of RF power there is a change of polarization of the target at the RF frequency, leading to no charging effects and hence non-conductive samples can also be sputtered. Because of continuous bombardment of electrons, the substrate temperature increases, so plastic and low melting materials cannot be used as substrates.

iii) Magnetron sputtering – In order to have denser plasmas at a lower operating pressures (~ 0.1mTorr) use of magnetic field was started in sputtering. Electrons experience a force $F = qv \times B$, perpendicular to their direction of motion, which leads to a circular motion of the electrons in the magnetic field. Using this principle a magnetron device is fabricated. Due to this the effective path of electrons is increased. Normally the magnet is kept parallel to the cathode as shown in Fig.1.3a

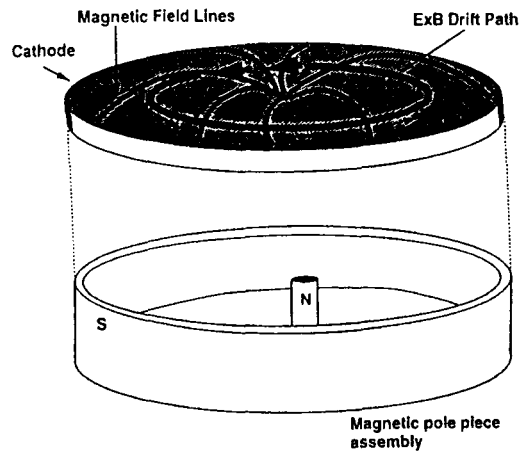


Fig.1.3a. Schematic diagram of a simplest magnetron assembly

In order to have a closed loop external magnetic field drift path for the secondary electrons, many different geometries of magnetrons have been developed. The most common of these is the rectangular configuration known as a racetrack magnetron and is shown in Fig.1.3b.

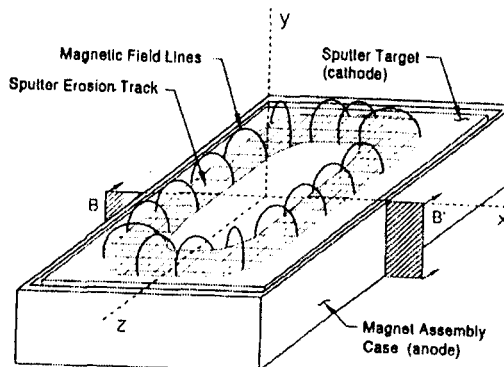


Fig.1.3b. Schematic diagram of a Racetrack magnetron

This geometry has some intrinsic advantages for the automated handling of parts. In any magnetron-sputtering set-up the area of the target which is exposed to magnetic field is only heavily sputtered. This leads to non-uniform deposition at the substrates. In order to overcome this multi-magnetron devices are used, as shown in Fig.1.3c.

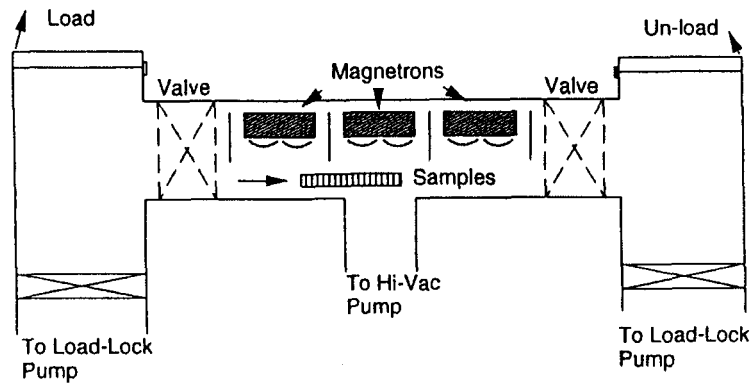


Fig.1.3c. Schematic diagram of multi-magnetron assembly

c) **Pulsed Laser Ablation Deposition (PLAD)** - The use of lasers for depositing films started with the need to make stoichiometric films of high T_c superconductors $\text{YBa}_2\text{Cu}_3\text{O}_{7.8}$ (YBCO). Fig 1.4 shows typical PLAD apparatus. The motivation behind the development of this technique is that the deposition of multicomponent materials can be done to exact composition of their targets by this technique. The growth rate of films is around $1\text{\AA}/\text{s}$ by this technique.

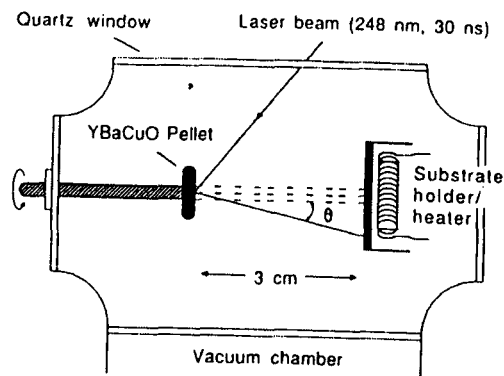


Fig.1.4 Schematic diagram of PLAD apparatus

Pulsed lasers like excimers, Nd:YAG and CO_2 have been used. Excimer laser proves to be the best because of their high power and small pulse as compared to other lasers. Recently compounds of formula $\text{Ln}_{1-x}\text{A}_x\text{MnO}_3$ (Ln = rare earth; A = alkaline earth; $x = 0.0 - 0.7$) have also been deposited.

d) **Molecular Beam Epitaxy (MBE)** - This is an advanced version of vacuum evaporation technique. In this technique the mean free path of the molecules or atoms of the material is increased by evaporating them at a pressure of the order of 10^{-10} torr. Under such conditions the mean free path of most of the materials is greater than the dimensions of the apparatus, hence they travel unperturbed and get deposited.

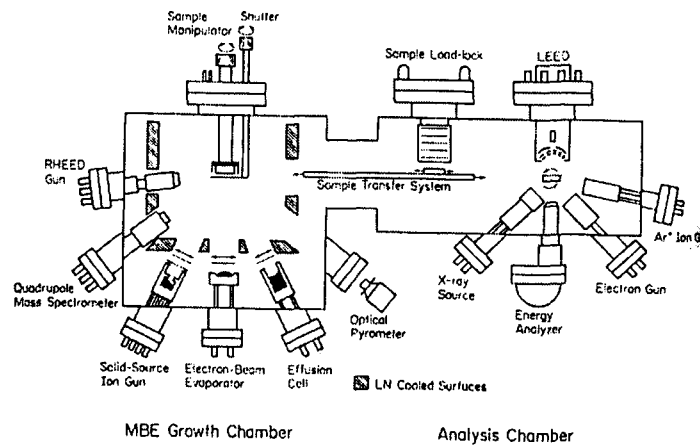


Fig.1.5. Schematic diagram of MBE apparatus

on the substrate. This technique has been successfully used at the laboratory level for the deposition of elemental and compound semiconductors like Si, GaAs and ZnSe. The growth in this technique can be monitored using quadrupole mass-spectrometer and in-situ RHEED. High T_c superconductors and other multicomponent materials have also been deposited from this technique by minor modifications in it. Some of the modifications in this technique are Metal-organic molecular beam epitaxy (MOMBE), Gas source molecular beam epitaxy (GSMBE) and chemical beam epitaxy. Fig.1.5 shows a single component MBE apparatus

1.2. Chemical vapor deposition (CVD)

It is the process where one or more volatile compounds decompose/react on a heated substrate to deposit a solid film. Organometallic and metal – organic compounds

are commonly used in this method, because they are highly volatile in nature. Large area deposition, conformal coverage and selective area deposition are some of the advantages that CVD offers over most of the PVD methods. Due to these advantages CVD of thin films of metals, semiconductors, dielectrics and ferroelectric materials has gained importance. Figs.1.6a and 1.6b show the mechanism and the block diagram of a CVD technique.

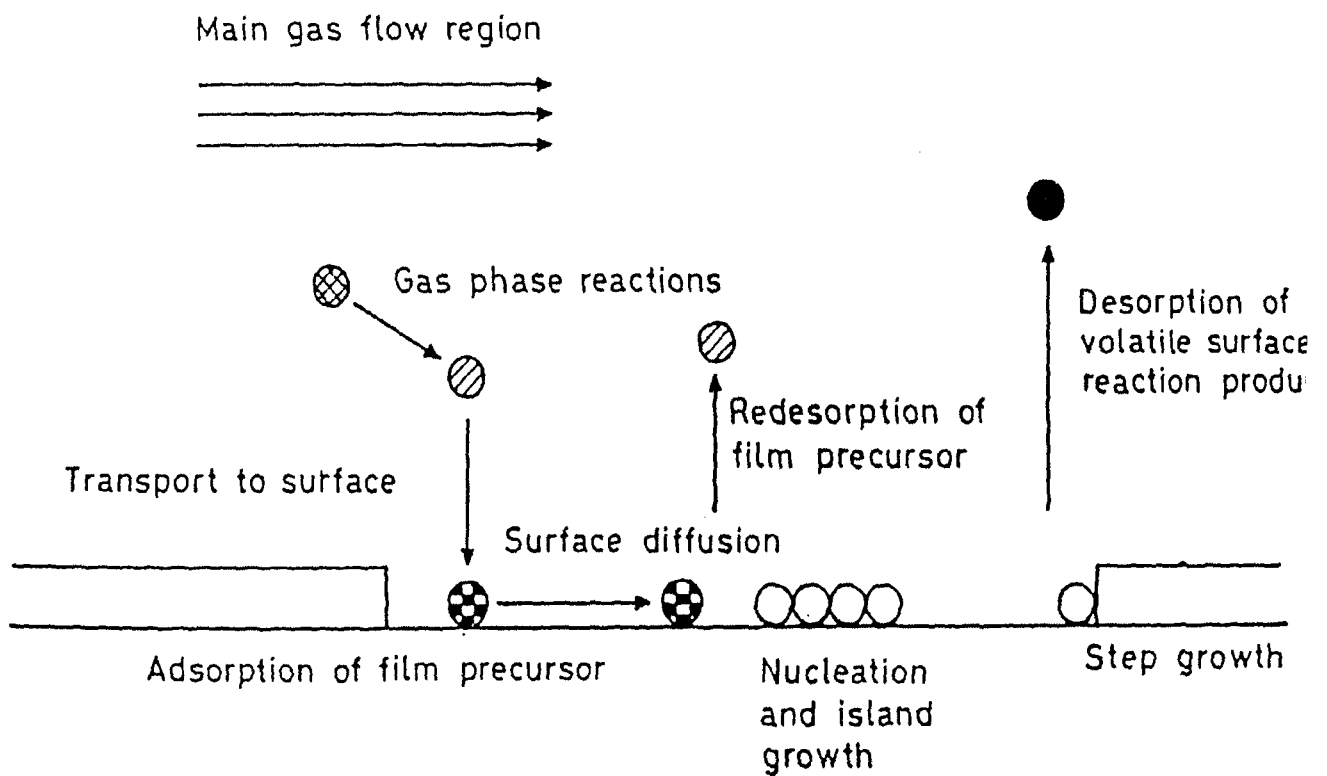


Fig.1.6a. Mechanism of a CVD process

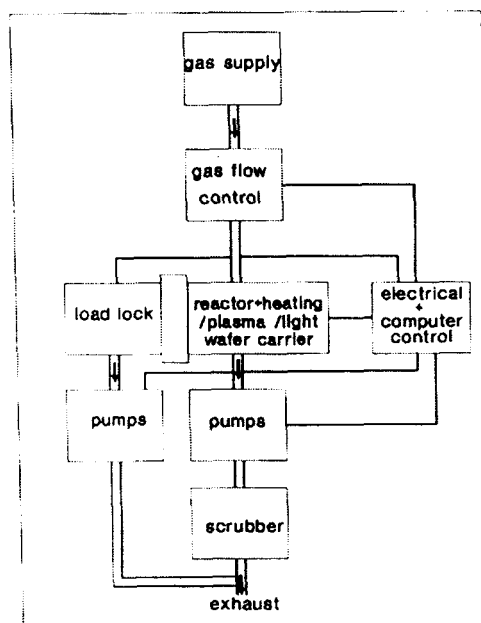


Fig.1.6b. Schematic diagram of a CVD reactor

On the basis of conditions employed there are various kinds of CVD techniques available and are given in table below.

Technique	Energy Promoting the reactions	Specifications
CVD(Thermal)	Thermal	Inorganic sources
MOCVD	Thermal	Organometallic sources
PECVD	Plasma	Lower temperature
PCVD	Light	Lower temperature, selected area
ALE	Thermal/Light	Monolayer control
NSP	Thermal	Low temperature , Selected area

a) **Thermally activated CVD process** – This process is initiated only with thermal energy (i.e. resistive heating, RF heating or by infrared heating). They are usually performed at normal or low pressure down to ultralow pressure. The sources mainly used are organic compounds. Fig.1.7 shows a thermal CVD set-up.

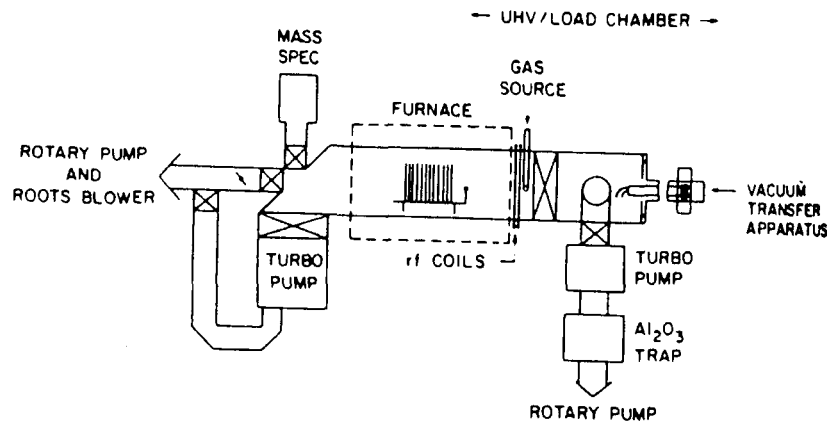


Fig.1.7. Schematic diagram of thermally activated CVD

b) **Metal-organic chemical vapor deposition (MOCVD)** – It is also a thermal CVD, but the sources are metal-organic solids or liquids. This technique has been most widely used in the epitaxial growth of II-VI and III-V group materials e.g. GaAs, GaN etc. and high T_c superconductors (YBCO). Recently compounds of formula $Ln_{1-x}A_xMnO_3$ (Ln = rare earth; A =alkaline earth) have also been deposited. Fig. 1.8 shows typical MOCVD set-up.

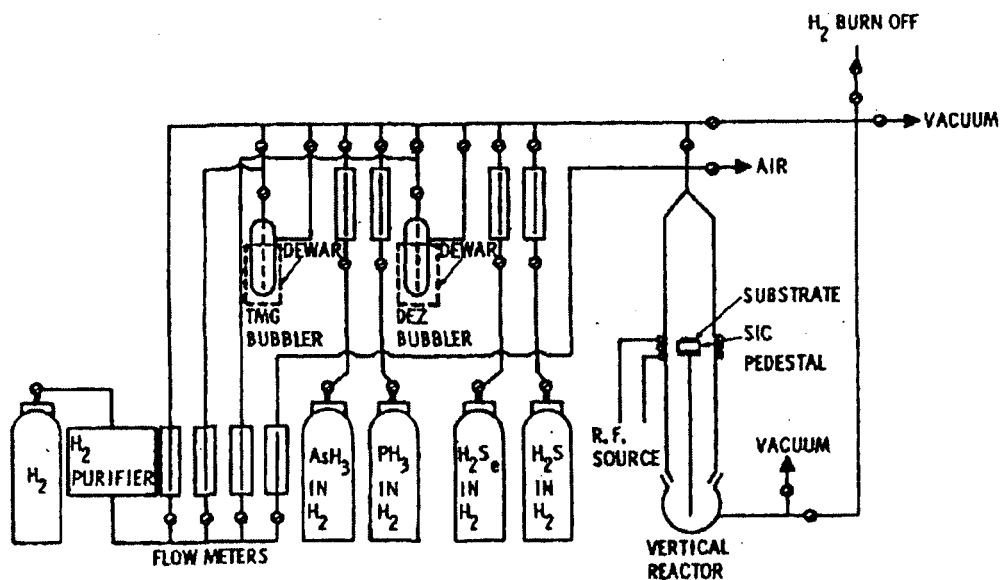


Fig.1.8. Schematic diagram of MOCVD set-up

(c) **Photo-assisted CVD (PCVD)** – This technique uses light to enhance the reaction rate. The purpose of radiation is either to do local heating of the wafer or to do a

photochemical reaction. In a photochemical reaction the reactant gases undergoes photolytic reactions. Fig.1.9 shows the PCVD set-up.

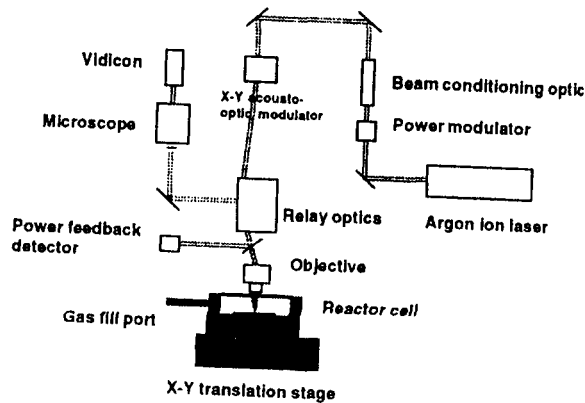


Fig.1.9. Schematic diagram of a PCVD reactor

- b) **Plasma-enhanced CVD (PECVD)** – This technique uses a plasma to ionize and dissociate gases. This enhances the growth rate, allowing the deposition processes at much lower temperature than in thermal CVD. PECVD has several features in common with low pressure CVD such as the pressure range, sources and films to be deposited. It is commonly used for depositing SiO_2 and Si_3N_4 .
- c) **Atomic layer Epitaxy (ALE)** – This is a relatively new approach for the thin film deposition. In ALE the reactants are supplied onto the growing surface sequentially one at a time. At each sequence the surface is saturated, resulting in the formation of one monolayer. The desired thickness of thin films can be realized by counting the number of reaction sequences in the process. It has been employed to deposit II-VI, III-V materials, oxides, nitrides and sulfides. Fig.1.10a and b shows the formation of a compound AB directly and from its precursors AX_n and BY_n . These precursors arrive one at a time then pyrolysis is done with the help of radiation (commonly high temperature halogen lamp) and after this the second material arrives. Same pyrolysis processes are carried out for this precursor also and thus layer by layer deposition takes place.

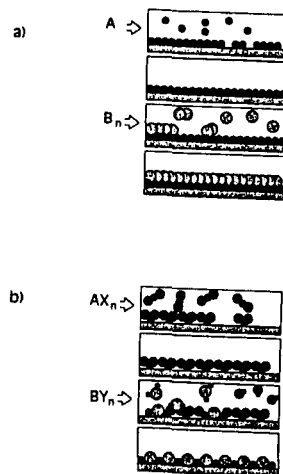


Fig.1.10. Mechanism of the simplest ALE process

d) **Nebulized spray pyrolysis (NSP)**- Spray pyrolysis has been used extensively to deposit films and to make powders. The problem with spray pyrolysis is that the droplet size is big (~1mm dia) and is also not uniform in the spray. In order to overcome these problems, the technique of nebulized spray pyrolysis⁶⁻⁸ or pyrosol process was developed. It is a technique, which has gained importance in recent years. The apparatus basically consists of two chambers, nebulization chamber and furnace chamber. A solution commonly containing a organometallic precursor is atomized with the help of a PZT transducer which vibrates at a frequency of 1.72 MHz. On vibrating the PZT transducer, the acoustic waves are generated and are transmitted to the solution – gas interface, leading to the formation of a geyser, which breaks the solution at the tip and forms a fine mist. This mist is then transferred to the furnace chamber with the help of a carrier gas. (Droplet size in the mist ~ 1 micrometer). In the pyrolysis chamber, substrate is maintained at a desired temperature and as soon as the mist reaches the substrate, a pyrolysis reaction takes place and the required film is formed.

In this thesis, results of the investigations of thin films of copper, cobalt, granular copper-cobalt alloys and rare earth manganates prepared by nebulized spray pyrolysis are presented. The scope of these investigations is described below.

2. SCOPE OF THE PRESENT INVESTIGATIONS

2.1 Copper films

The demand of higher data density storage media has resulted in miniaturization of electronic circuits. This denser media needs a very high speed of processing which should have a minimum time of signal delay. This can only be achieved by having better interconnects in the circuits. Copper is a promising material for metallization in ultra-large scale integrated circuits, such as dynamic random access memories because of its low resistivity, high electromigration resistance and high melting point compared to aluminium and its alloys. Copper films are therefore emerging as useful materials in new technologies. Till now copper has been ignored as interconnect material because of several reasons: (i) Lack of an anisotropic low temperature copper etch process; (ii) High diffusion coefficient of copper in Si and SiO₂; (iii) Low oxidation resistance and (iv) It is a poison to active device area due to formation of deep acceptor level traps in forbidden energy gaps of Si.

In order to overcome these problems, intense research has been carried out by various workers. One of the problems in this area relates to the method of deposition of copper. Physical vapor deposition (PVD) techniques such as sputtering or evaporation employed for depositing films are limited by line of sight deposition and are susceptible to shadowing, poor uniformity and extended defects⁹⁻¹¹, making chemical vapor deposition (CVD) a more desirable choice in such applications¹²⁻¹⁵. CVD has also other advantages of uniform large area coverage and certain processing benefits such as low temperature deposition, deposition selectivity and conformal coverage. Furthermore,

precursors for the CVD process can be generally obtained in high purity to allow films to be deposited with the low impurity levels required in the electronic devices. Several Cu β -diketonates have been used as precursors for CVD of copper films in the literature¹²⁻¹⁵ and CVD has been shown to be viable with both Cu(I) and Cu(II) β -diketonates. We have made good copper films by the simple, low-cost solution based chemical technique of nebulized spray pyrolysis. We have used three β -diketonates of copper(II), viz., Cu(acac)₂ (bis-acetylacetonato copper), Cu(hfac)₂ (bis-hexafluoroacetylacetonato copper) and Cu(dpm)₂ (bis-dipivaloylmethanato copper) as precursors in the present study. We have carried out a comparative study of the crystallinity, morphology, growth kinetics, electrical resistivity and environmental stability of the copper films obtained by the nebulized spray pyrolysis of these precursors. In addition, we have estimated the grain boundary and other contributions to the observed resistivity on the basis of known models.

2.2 Cobalt and granular Copper-Cobalt films

Thin films of cobalt are known to be useful in memory elements and in microelectronics because of their low resistivity and high oxidation resistance. Although cobalt films have been obtained by thermal evaporation and sputtering techniques, their study has been rather limited. Recently, Li *et al*¹⁶ have reported the study of cobalt films deposited by thermal evaporation and chemical vapor deposition (CVD) of β -diketonate compounds. These workers were concerned with the magnetic properties of Co films with respect to their surface roughness. Maruyama¹⁷ deposited Co films of varying thickness by the CVD technique and studied their electrical transport properties with varying thickness. We have deposited thin films of cobalt by nebulized spray pyrolysis using Co (II) acetylacetonate as precursor and ultra high pure H₂ as the carrier gas. These films were grown on Si(100) as well as on borosilicate glass. The films showed hcp and fcc

single and mixed phases on Si(100) and glass substrate at different deposition conditions. Electrical resistivity and magnetic hysteresis measurements were carried out on the Co films.

Copper-cobalt granular films are being investigated extensively in recent years because of the giant magnetoresistance (GMR) exhibited by them. These films have been prepared by dc sputtering¹⁸, magnetron sputtering^{19,20} and melt spinning²¹. We have deposited granular copper-cobalt alloy thin films by nebulized spray pyrolysis using similar conditions as those with cobalt. The compositions of $\text{Cu}_{1-x}\text{Co}_x$ are $x=0.2$ and 0.5 . The films showed a mixed phase of copper and cobalt in the as deposited form but showed a phase separation when annealed in hydrogen. Magnetoresistance properties of the granular films were measured.

2.3 Films of charge-ordered rare earth manganate

Rare earth manganates of the formula $\text{Ln}_{1-x}\text{A}_x\text{MnO}_3$ (Ln=rare earth, A=alkaline earth) exhibit important phenomena such as colossal magnetoresistance (CMR) and charge ordering^{22,23}. Charge-ordering in the manganates is especially interesting since it competes with double exchange, giving rise to interesting properties. Charge ordering is favored in certain compositions such as those with $x = 0.5$ and is associated with insulating behavior and in certain instances, antiferromagnetism as well. Charge-ordering in these materials is very sensitive to the average radius of the A-site cations, $\langle r_A \rangle$. Two types of charge-ordering can be distinguished in the manganates²⁴. In manganates such as $\text{Nd}_{0.5}\text{Sr}_{0.5}\text{MnO}_3$ ($\langle r_A \rangle = 1.24\text{\AA}$) with a relatively large average radius of the A-site cations, $\langle r_A \rangle$, a ferromagnetic metallic (FMM) state ($T_c = 250\text{ K}$) transforms to a charge-ordered (CO) state on cooling to $\sim 150\text{ K}$ ²⁵. Manganates with a small $\langle r_A \rangle < 1.17\text{\AA}$, do not exist in the FMM state at any temperature, but instead are charge-ordered at relatively high temperatures. The CO state in a manganate with a relatively large A-site ion radius ($\langle r_A \rangle$

$\geq 1.17\text{\AA}$) can be transformed to the FMM state by the application of magnetic fields. On the other hand, even large magnetic fields (≥ 40 tesla) have negligible effect on the CO state of $\text{Y}_{0.5}\text{Ca}_{0.5}\text{MnO}_3$ with a $\langle r_A \rangle$ of 1.13\AA . The CO state in single crystals of $\text{Pr}_{1-x}\text{Ca}_x\text{MnO}_3$ has been transformed to the FMM state by applying electric fields or by laser irradiation^{26,27}. An examination of the literature shows that there has been little or no effort to prepare thin films of the charge-ordered manganates, although thin films of the manganates showing CMR have been prepared by various means²⁸⁻³¹. We report the successful preparation of thin films of the charge-ordered manganates, $\text{Nd}_{0.5}\text{Ca}_{0.5}\text{MnO}_3$ (NCM), $\text{Y}_{0.5}\text{Ca}_{0.5}\text{MnO}_3$ (YCM) and $\text{Nd}_{0.5}\text{Sr}_{0.5}\text{MnO}_3$ (NSM) (with $\langle r_A \rangle$ values of 1.17\AA , 1.13\AA and 1.24\AA respectively) on Si(100) and LaAlO_3 substrates by employing nebulized spray pyrolysis of organometallic precursors. More importantly, we have investigated the electric current-induced transition from the insulating CO state to the metallic state in these films. It is noteworthy that the insulator-metal transition in the thin films of the CO manganates is brought about by passing small currents. Even YCM with a very small $\langle r_A \rangle$ exhibits this phenomenon although high magnetic fields have no effect on the CO state in this material.

The charge-ordered manganate films were doped with Cr^{+3} on the Mn site since Cr^{+3} is known to melt the charge-ordered state into the ferromagnetic metallic states³¹. Electrical resistivity measurements on the films of the composition $\text{Ln}_{1-x}\text{A}_x\text{Cr}_{0.03}\text{Mn}_{0.97}\text{O}_3$ (Ln = Nd, Gd and Y; A = Ca and Sr) were carried out to see the charge-ordered state is affected by Cr^{+3} .

3. EXPERIMENTAL

The films of metals and metal oxides were prepared employing the simple, low cost, solution based chemical technique called nebulized spray pyrolysis.

3.1. Nebulized Spray Pyrolysis

Pyrolysis of sprays is a well-known method for depositing films and for making fine powders. A novel improvement in this technique is the so-called pyrosol process or nebulized spray pyrolysis involving the transport and subsequent pyrolysis of a spray generated by an ultrasonic atomizer as demonstrated by Joubert and coworkers^{8,32,33}. Wold and coworkers³⁴⁻³⁷ have employed this method to prepare thin films of a variety of oxides. This method seem to be an excellent compromise for obtaining thin films economically, which are adhesive homogeneous and with excellent physical properties.

The advantage of this technique is the ultrasonic atomization process. When a high frequency (100 kHz to 10 MHz) ultrasonic beam is directed at a gas-liquid interface, geyser forms at the surface and the height of the geyser is proportional to the acoustic intensity and the physical properties of the liquid (vapor pressure, viscosity and surface tension). The generation and cavitation at the gas-liquid interface accompany its formation.

(a) Ultrasonic atomization : If a liquid is irradiated ultrasonically, above a certain excitation power threshold, leads to the atomization of fine droplets forming a spray. The correlation between the capillary wavelength (λ_c) at the liquid surface and the mean diameter of the atomized droplets (D) is one of the fundamental principles of ultrasonic atomization

$$D = \alpha \lambda_c \quad (1)$$

Where α is the proportionality constant. Based on Kelvin's equation, the capillary wavelength can be written as,

$$\lambda_c = (8\pi\sigma / \rho f^2)^{1/3} \quad (2)$$

where σ is the surface tension of the liquid, ρ its density and f the ultrasonic excitation frequency. The droplet diameter is therefore expressed in terms of σ , ρ and f .

$$D = \alpha (8\pi\sigma / \rho f^2)^{1/3} \quad (3)$$

In the case of water, the most probable diameter of the atomized droplets varies from 2 to 30 microns when the frequency varies from 3MHz to 70kHz. In addition, the frequency dependence expressed by the relation (3) gives rise to a very narrow distribution in terms of number and volume of atomized droplets as shown in Fig.3.1a. This narrow distribution over more conventional pneumatic atomization techniques which give droplets whose size is difficult to control and a spray that always contain a certain percentage of large droplets Fig.3.1b⁸.

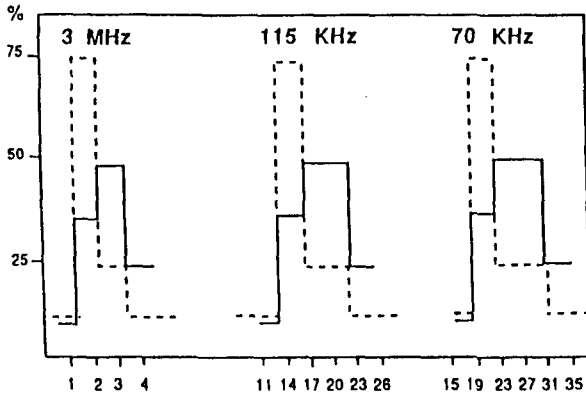


Fig.3.1a. The distribution of droplet diameter versus volume percentage for different frequencies for nebulized spray. (adapted from ref.8)

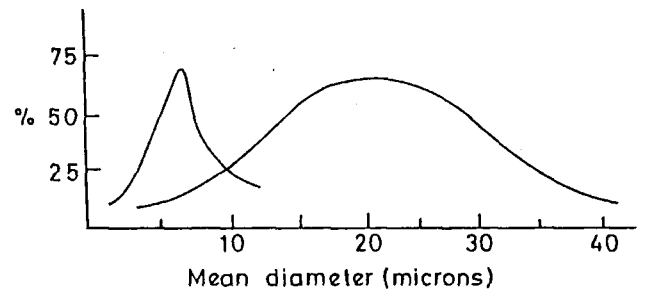


Fig.3.1b The distribution of droplet diameter for pneumatic spray

The relation clearly shows that the mean diameter of the atomized droplets depends not only on the excitation frequency, but also on the characteristics of the irradiated liquid. The same is true for the quantity of the spray produced. It has been shown that, at constant carrier gas feed and flow rate, this production was an increasing function of the ratio,

$$\gamma = p_s / \sigma \eta \quad (4)$$

where p_s represents the saturated vapor pressure of the liquid, σ its surface tension and η its dynamic viscosity. It is therefore theoretically possible to predict the atomization kinetics of the liquid if its physical properties are known.

(b) Atomization process: The source liquid containing the relevant cations in the form of salts dissolved in an organic solvent is kept in the atomization chamber. A piezoelectric transducer (PZT) crimped to the base of the chamber is connected to a high frequency (1.72MHz) generator of 30-100 watts power. By varying the voltage (with the frequency fixed at a value close to the resonant frequency of the PZT ceramic), the intensity of the geyser which appears at the liquid surface, where the acoustic waves are focused, also varies. Liquid atomization occurs when the amplitude of the acoustic vibrations exceeds a certain value, considered to be a threshold for that liquid. Just above this threshold the mist produced is intermittent and corresponds to irregular disintegration of the geyser. At much higher values than the threshold, mist emission becomes continuous and regular. A constant level burette is used to ensure liquid level stability in the chamber and for in-situ measurement of the volume of the deposited liquid. The liquid height above the transducer is equivalent to the load of the PZT transducer and the mist formation also depends on this height.

During the atomization process, the liquid is heated at the top of the geyser where the acoustic intensity is maximum. At this point, the temperature exceeds 375K. Consequently a small portion of the atomized spray may change into the vapor state, which is detrimental to the spray homogeneity. To avoid this problem, the nozzle carrying the mist from the atomization chamber to the reactor must be designed sufficiently narrow and long to leave the vapors to re-condense into droplets during the transport stage. However, the nozzle should not be too long as collisions between the

droplets during the transport may give rise to a considerable change in size distribution through a coalescence process. The length and diameter of the pyrosol reactor are 50cm and 3cm respectively.

(c) Pyrolysis: The pyrolysis reaction, which determines the deposition kinetics, takes place when the spray passes near the hot substrate. The temperature is controlled by a thermocouple placed at the heating support-substrate interface. This method of measurement and substrate temperature control is the one most frequently used as it enables in-situ measurement without disturbing the deposition process.

Depending on the substrate temperature, several deposition processes can be considered and can be described in a simplified form by one of the four schemes (Fig.3.2)

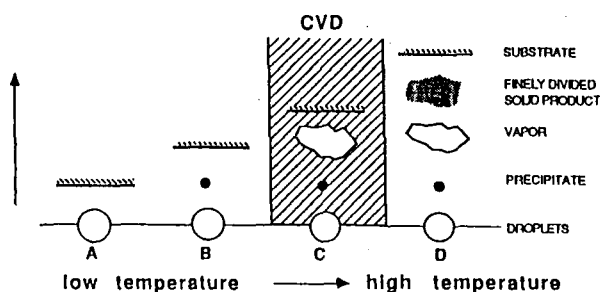


Fig.3.2. Various deposition reaction schemes for the nebulized spray pyrolysis process (Adapted from ref.8)

- (a) At low temperatures (case A), the droplets reach the substrate in liquid state. The solvent in which the source compounds dissolved slowly evaporates leaving a finely divide precipitate on the substrate.
- (b) At high temperatures (case B), the solvent has time to evaporate before reaching the substrate and the precipitate impacts the substrate in the solid state.
- (c) At still high temperatures (case C), the solvent evaporation and precipitate sublimation occurs in succession. The vapors obtained will diffuse towards the

substrate where they react chemically in heterogeneous gas-solid phase to give the final compound. This is a typical case of CVD.

- (d) At excessively high temperatures (case D), the chemical reaction takes place before the vapor reaches the substrate. The product of this chemical reaction deposits on the substrate in fine powder form.

Although it is possible to obtain a coating in each case, the adherence is very poor in cases A, B and D. The adherence can be improved by appropriate annealing, although the resulting films will never have optical quality. However, the films obtained with the reaction process C, have excellent adherence and high optical quality, without the need for annealing. These deposits are perfectly crystalline. It is easy to see the advantage of a narrow droplet size range likely to react chemically before reaching the substrate, thereby giving a homogeneous deposits³⁷.

(d) Apparatus: The schematic diagram showing different parts of the nebulized spray pyrolysis apparatus fabricated by us for is shown Fig.3.3. It consists of two independent zones.

(a) The atomization chamber

(b) The pyrolysis chamber

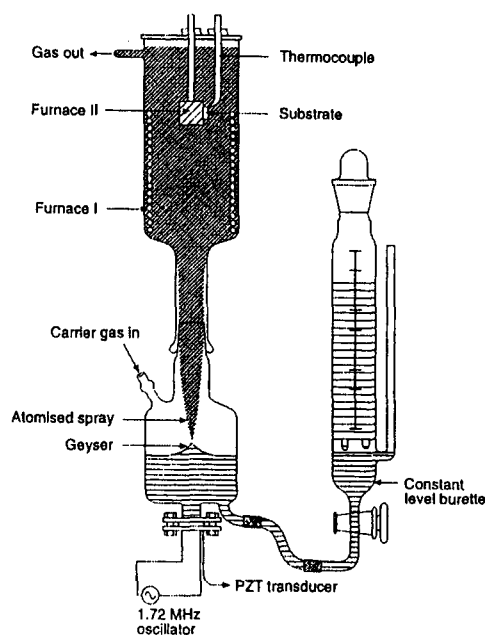


Fig.3.3. Schematic diagram of the apparatus used for nebulized spray pyrolysis

The atomization chamber is constructed such that the bottom of the chamber is having 20mm diameter and 1mm thickness. The special feature of our design is that the transducer is in direct contact with the liquid, thereby the energy transfer to the liquid is highest when compared to the non-contact methods. The disadvantage being the liquid pH has to be maintained at around 7. The liquid level in the atomizer chamber is maintained by using a constant level burette.

A carrier gas introduced through a side port transports the spray produced in the first chamber. The second zone is a long glass tube consisting of a heater (nichrome wire wounded on a ceramic tube), a substrate holder and a chromel-alumel thermocouple fixed to the substrate holder. The pyrolysis reaction product consists of a thin film, whose composition, adherence and morphology depend on the experimental conditions. These two zones can be completely dismantled for cleaning purposes. They are made off borosilicate glass as it gives excellent heat resistance and ease of fabrication. One of the

features that make the whole process so simple is that this technique does not employ vacuum systems.

Ultrasonic atomization is accomplished by using an appropriate transducer (PZT) located at the bottom of the liquid container. The atomized spray is transported to the heater chamber by the carrier gas and is deposited on a suitable solid substrate. I have deposited films of metals and metal oxides which are described in detail below.

3.2. Copper Metal Films

Copper films were deposited using a home made nebulized spray pyrolysis apparatus described previously (section 3.1). A solution containing the copper precursor in methanol solvent (concentration $\sim 1\text{mM}$) was nebulized making use of a PZT (1.72 MHz) transducer. We in our study of copper films have used Cu(II) β -diketonates namely Cu(acac)₂ (bis-acetylacetonato copper), Cu(hfac)₂ (bis-hexafluoroacetylacetonato copper) and Cu(dpm)₂ (bis-dipivaloylmethanato copper). The structures of all the three compounds are shown in Fig.3.4.

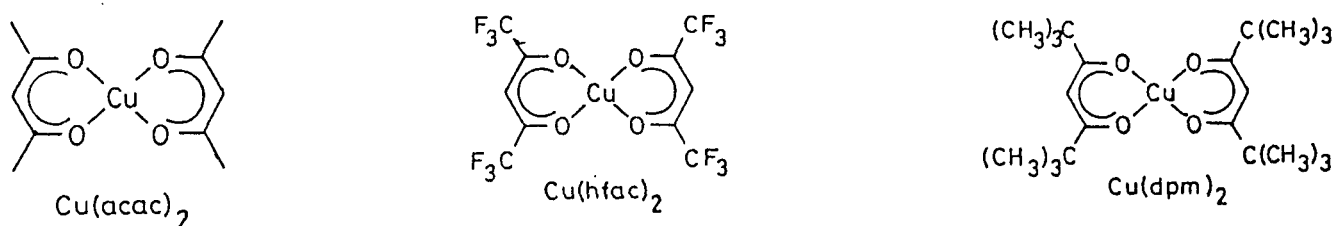


Fig.3.4. Structures of various precursors employed

All the precursors were prepared by using the commercially obtained β -diketonate ligands and Cu (II) chloride salts in ammonium hydroxide (NH₄OH) medium. Bases like sodium hydroxide and other alkali bases were avoided because the alkaline cation also undergoes a chelation reaction and lead to contamination of the products. In the preparation of all the precursors the ligands were dissolved in methanol and then NH₄OH is added to this solution in excess in order to make ammonium salt β -diketonate and

simultaneously dissolve it in NH_4OH to make a clear solution. This solution was then added to the Cu (II) chloride solution in water with constant stirring of the mixture with the pH maintained at 7 and then left for 1 hr. After 1 hr the solution is filtered and the precipitate was thoroughly washed with water in order to remove unreacted chloride salts from the precursor. This precipitate was kept for drying for 24 hrs over P_2O_5 in vacuum.

Films were deposited on Si (100) substrates at substrate temperatures of 523K-673K for 3-12 hrs. A mixture of ultrahigh pure N_2 and H_2 (100 sccm) was used as the carrier gas to transport the nebulized precursor with a typical gas flow rate of 1-1.5 l / min. In order to avoid the formation of oxide, the growth chamber was thoroughly purged with N_2/H_2 mixture before and after the deposition run. After the deposition is complete the films were kept in vacuum in order to minimize the rate of oxidation.

The deposited films were studied by X-ray diffraction using a Seifert (xrd, xdl, θ - θ , Cu target) instrument. Conventional θ - θ scans were collected with a Bragg-Brentano goniometer and high resolution (169 eV) Si(Li) solid state detector with 0.5 mm/1 mm slits. The surface morphology of the films was observed by scanning electron microscopy (SEM) with a Leica S-440 i SEM. The film thickness was confirmed by cross-sectional scanning electron microscopy. The EDX analysis was done using Links ISIS of Oxford instrument. Scanning tunneling microscope (STM) images were obtained with Nanoscope II (Digital Instruments, USA) to study the surfaces of some of the copper films. STM images were recorded at room temperature (in air) in constant current mode using Pt-Ir tips employing a bias voltage and a tunneling current of 100-500 mV and 0.2-1 nA, respectively. Prior to scanning the film sample, STM was calibrated by imaging a freshly cleaved highly oriented pyrolytic graphite (HOPG) surface. Electrical resistivity of the deposited films was measured by the four-point probe method.

3.3. Cobalt and granular copper-cobalt alloy films

Cobalt films and copper-cobalt (Cu-Co) granular alloy films were deposited using the home-built nebulized spray pyrolysis apparatus described in section 3.1. A solution of $\text{Co}(\text{acac})_2$ (bis-acetylacetonato cobalt) in methanol solvent ($\sim 1\text{mM}$) was nebulized using the PZT transducer (1.72MHz). Similarly a solution containing a mixture $\text{Cu}(\text{acac})_2$ (bis-acetylacetonato copper) and $\text{Co}(\text{acac})_2$ (bis-acetylacetonato cobalt) of required composition was used to deposit Cu-Co granular alloy films. Both the precursors were prepared using commercially obtained ligand and metal chlorides as explained in section 3.2. The composition of the films deposited were $\text{Cu}_x\text{Co}_{(1-x)}$ ($x = 0.5$ to 0.9). The films were deposited on Si(100) as well as on borosilicate glass at substrate temperatures ranging from 598 K to 673 K for 7-9 hrs. Zero grade hydrogen was used as carrier gas to transport the nebulized precursor with a typical flow rate of 1-1.5l/min. In order to avoid the formation of any oxide the growth chamber was purged with hydrogen gas before and after the run. The deposited films were examined by XRD, SEM, electrical transport properties using four probe resistivity technique with a constant current source of Keithley model-220, Lakeshore autotuning temperature controller and digital multimeter Keithley model-2000. The magnetic properties were studied using Lakeshore VSM 7300 vibrating sample magnetometer.

3.4. Charge-ordered rare earth manganate films

Thin films of the charge ordered manganates²²⁻²⁴ of the formula $\text{Ln}_x\text{A}_{1-x}\text{MnO}_3$, where (Ln = Nd, Gd and Y; A = Ca and Sr; and $x = 0.5$) were deposited on Si(100) as well as on LAO(100) single crystal substrates by employing nebulized spray pyrolysis described in section 3.1. The precursors employed were $\text{Nd}(\text{acac})_3$ (tris acetylacetonato neodymium), $\text{Gd}(\text{acac})_3$ (tris acetylacetonato gadolinium), $\text{Y}(\text{acac})_3$ (tris acetylacetonato yttrium), $\text{Ca}(\text{acac})_2$ (bis acetylacetonato calcium) and $\text{Mn}(\text{acac})_3$ (tris acetylacetonato

manganese) for $\text{Nd}_{0.5}\text{Ca}_{0.5}\text{MnO}_3$, $\text{Gd}_{0.5}\text{Ca}_{0.5}\text{MnO}_3$ and $\text{Y}_{0.5}\text{Ca}_{0.5}\text{MnO}_3$ films. For $\text{Nd}_{0.5}\text{Sr}_{0.5}\text{MnO}_3$ films $\text{Nd}(\text{dpm})_3$ (tris dipivaloylmethanato neodymium), $\text{Sr}(\text{dpm})_2$ (bis dipivaloylmethanato strontium) and $\text{Mn}(\text{dpm})_3$ (tris dipivaloylmethanato manganese) were employed. All the precursors were prepared from commercially available ligands and chloride salts of the required elements. The films of ~ 1000 nm thickness were deposited at 650 K by using air as the carrier gas (1.5 liters/min).

The films so obtained were heated at 1000 K in oxygen. These films were characterized by employing X-ray diffraction and scanning electron microscopy. The compositions of the films as determined by EDAX were close to the stated compositions. The films deposited on Si(100) showed polycrystalline nature while those deposited on LAO were oriented along the (100) direction. The orthorhombic lattice parameters of the materials agree with the literature values. Temperature-dependent resistivity measurements were carried out by employing close cycle refrigerator and sputtered gold electrodes. These gold electrodes had a constant distance of separation between them and sputtered with help of a mask. Typical separations were 1mm, 0.5mm and 0.2mm and the length of electrodes were 10mm, 8mm and 5mm.

4. RESULTS AND DISCUSSION

4.1. Copper films

We have carried out a comparative study of crystallinity, morphology, growth kinetics, electrical resistivity and environmental stability of copper films obtained by nebulized spray pyrolysis of $\text{Cu}(\text{acac})_2$ (bis-acetylacetonato copper), $\text{Cu}(\text{hfac})_2$ (bis-hexafluoroacetylacetonato copper) and $\text{Cu}(\text{dpm})_2$ (bis-dipivaloylmethanato copper). In addition, we have estimated the grain boundary and other contributions to the observed resistivity on the basis of known models.

(a) X-ray diffraction studies: Fig.4.1 shows x-ray diffraction patterns of Cu films deposited from $\text{Cu}(\text{acac})_2$, $\text{Cu}(\text{hfac})_2$ and $\text{Cu}(\text{dpm})_2$ precursors on Si (100) substrates at 673 K for 12 hr. All the patterns show polycrystalline Cu (111) and Cu (200) reflections, with no indication of any oxide phase within the limits of detection. The peak-height intensity ratio of Cu (111) and Cu (200) reflections is 2.17 in a standard Cu powder sample (JCPDS File No. 4-836). The observed peak height ratios ($I_{(111)}/I_{(200)}$) for our Cu films are however, much larger than the polycrystalline reference and are 11.6, 3.9 and 15.8 respectively for films deposited from $\text{Cu}(\text{acac})_2$, $\text{Cu}(\text{hfac})_2$ and $\text{Cu}(\text{dpm})_2$ precursors. This observation clearly suggests that for the Cu films derived from $\text{Cu}(\text{dpm})_2$, the degree of preferred (111) orientation is higher than that obtained from $\text{Cu}(\text{acac})_2$ or $\text{Cu}(\text{hfac})_2$. The films from $\text{Cu}(\text{hfac})_2$ show the least preference for (111) orientation of the film. These differences in the orientation preference of Cu films deposited from different precursors arise from the differences in the energetic of the surface reactions.

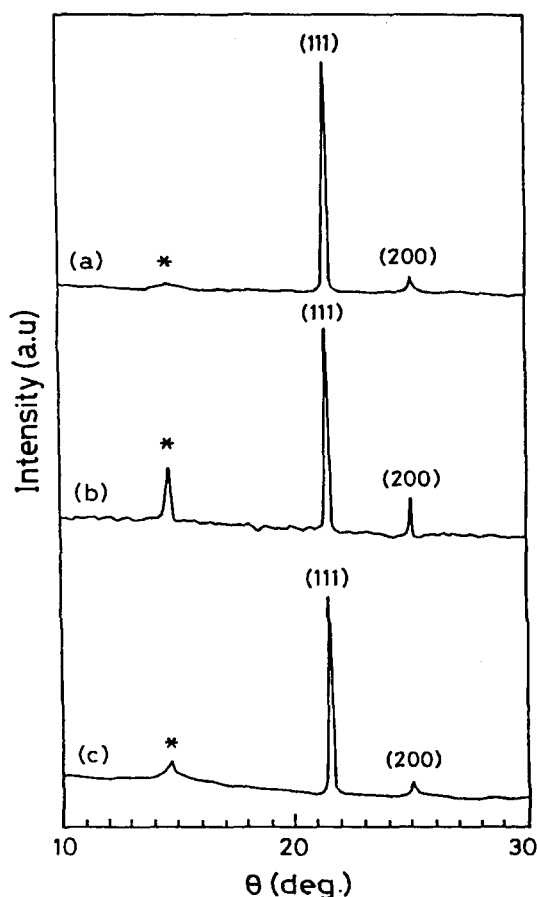


Fig.4.1. XRD patterns of Cu films obtained (a) $\text{Cu}(\text{acac})_2$, (b) $\text{Cu}(\text{hfac})_2$, (c) $\text{Cu}(\text{dpm})_2$
 `*` denotes $\text{Si}(100)$ reflection

(b) Morphology: SEM images of the Cu films deposited at 673 K for 12 hrs using different precursors is shown in Fig.4.2. The variation of the surface morphology of the films with precursor employed is evident. The films from $\text{Cu}(\text{acac})_2$ [Fig.4.2 (a)] and $\text{Cu}(\text{dpm})_2$ [Fig.4.2 (b)] have a uniform and smooth morphology. The films from $\text{Cu}(\text{hfac})_2$ [Fig.4.2 (c)], on the other hand exhibit a rough, highly porous microstructure with a wide distribution of grain sizes, with an average grain size of $\sim 500\text{nm}$. These observations can be clearly conformed from the high magnification SEM images of the films. In case of the films from $\text{Cu}(\text{hfac})_2$ [Fig.4.3 (c)] at a magnification of 2 KX only grains can be clearly seen, but on the other hand for the films obtained from $\text{Cu}(\text{dpm})_2$ [Fig.4.3 (b)], a smooth morphology is seen till 20 KX, and also for films of $\text{Cu}(\text{acac})_2$ grains are visible only at 6 KX [Fig.4.3 (a)]. The films deposited from $\text{Cu}(\text{acac})_2$ show comparatively higher growth rates resulting in the reduced surface mobility of the growth species and enhanced nucleation density. These films are

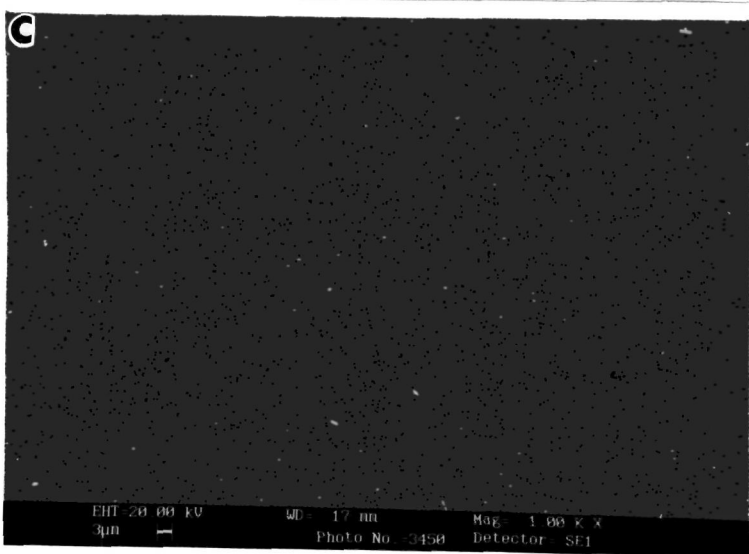
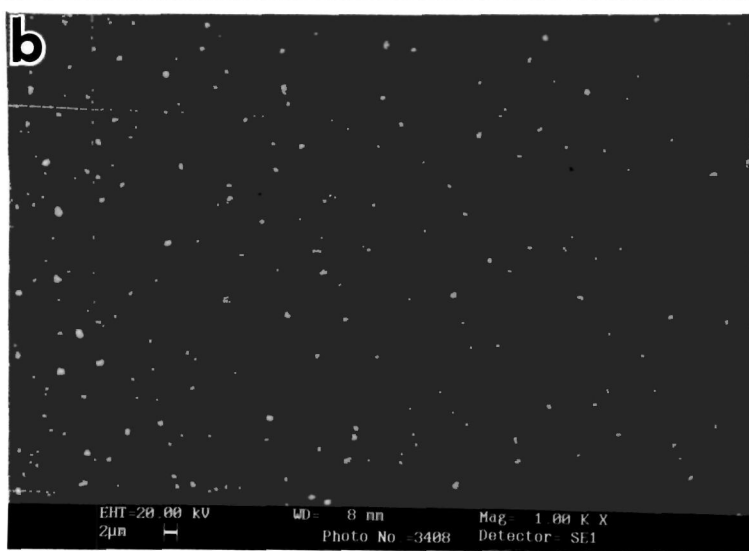
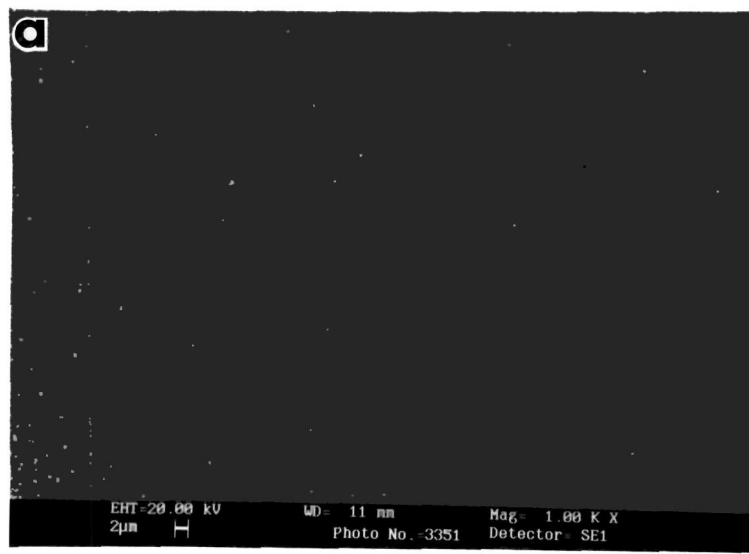
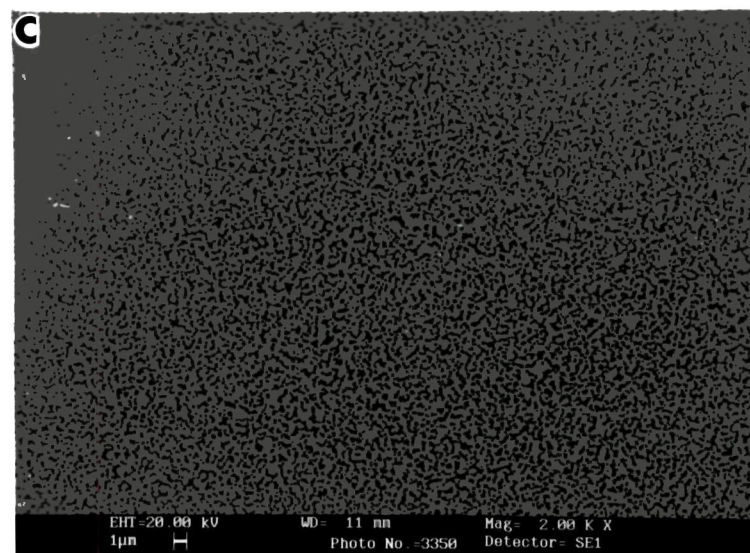
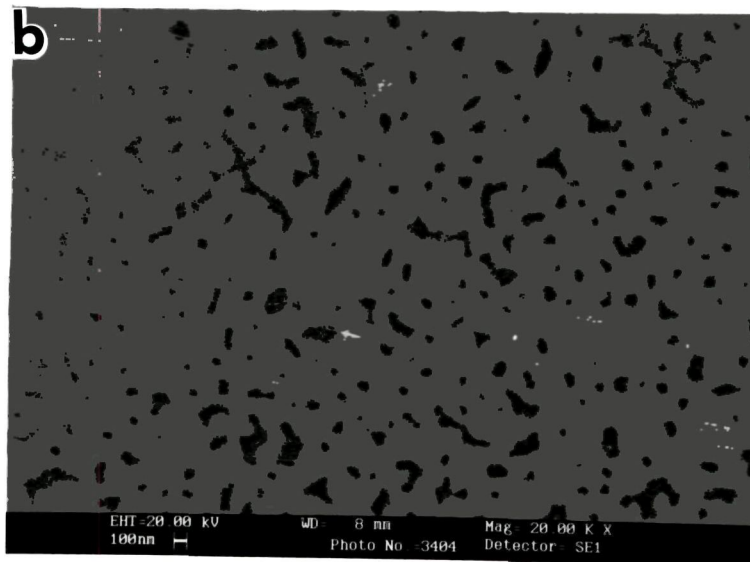
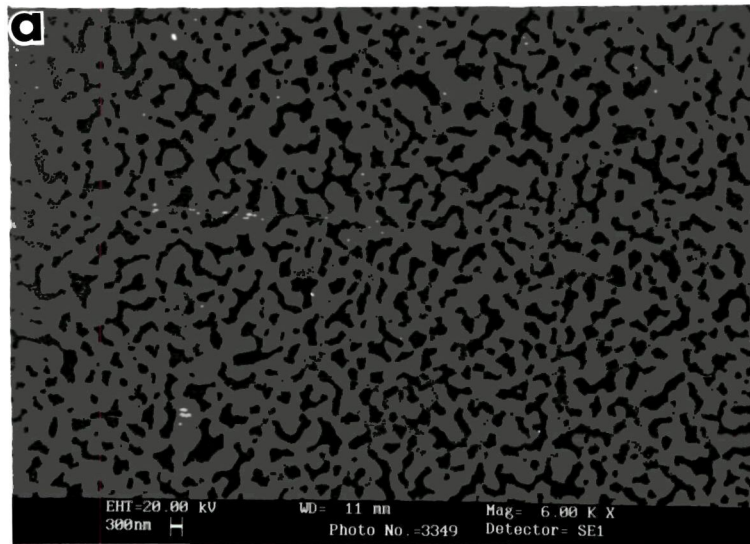


Fig.4.2. Low-magnification scanning electron micrographs of Cu films deposited at 673K from (a) $\text{Cu}(\text{acac})_2$, (b) $\text{Cu}(\text{dpm})_2$ and (c) $\text{Cu}(\text{hfac})_2$.

530.HITS
N99



JNCASR
ACC
No. - 3020
LIBRARY

Fig.4.3. High-magnification scanning electron micrographs of Cu films deposited at 673K from (a) $\text{Cu}(\text{acac})_2$, (b) $\text{Cu}(\text{dpm})_2$ and (c) $\text{Cu}(\text{hfac})_2$.

therefore relatively more dense and exhibit a smooth microstructure with high intergrain connectivity. This becomes evident from the cross sectional SEM images presented in Figs.4.4 (a) and (b). The films from $\text{Cu}(\text{hfac})_2$ are characterized by low growth rate, incorporate voids and hence show a less dense microstructure. The intergrain connectivity in the films from $\text{Cu}(\text{hfac})_2$ is poor because of this factor, as seen in the cross sectional SEM image of Fig.4.4(c). We obtained good copper films from $\text{Cu}(\text{acac})_2$ precursor from 573 K to 673 K. We could not obtain copper films from $\text{Cu}(\text{dpm})_2$ and $\text{Cu}(\text{hfac})_2$ precursors below 673 K.

As the films obtained from $\text{Cu}(\text{dpm})_2$ were extremely smooth and no grain were seen at high magnification in SEM, so we have carried out STM studies by employing Digital Nanoscope II scanning tunneling microscope was done on these films in order to know their morphology of these films. The topview and the surface plot (in 60° perspective) are presented in Fig.4.5 (a) and (b). The images reveal cauliflower like growth patterns. These images show orbicular agglomeration composed of small grains which appear to grow about a common central nucleation point. The average width of the agglomeration is around 400 nm while the grain size is ~ 40 nm. A typical agglomeration is marked as 'D-C-F-E' in Fig.4.5 (a) wherein 'C' is clearly seen as its nucleation point. A line profile taken across the 'D-C-F-E' shown in Fig.4.5 (c), reveals the nucleation point C as a central dark valley of ~ 20 nm depth. The 30-50 nm grains appearing as mounds grow around this point. The root mean square (rms) roughness within the agglomeration is 4.88 nm and within the grain is 1.17 nm.

The variation of average grain size, $\langle D \rangle$, for the films obtained from $\text{Cu}(\text{acac})_2$, determined from statistical analysis of different SEM images, is shown as a function of the deposition temperature in Fig.4.6. At a low deposition temperature of 523 K, the average grain size is ~ 76 nm, with a small number of grains of sizes above 100 nm. With the increasing deposition temperature, an increasing number of larger grains is observed. These grains grow at the expense of smaller grains and have sizes significantly above the main

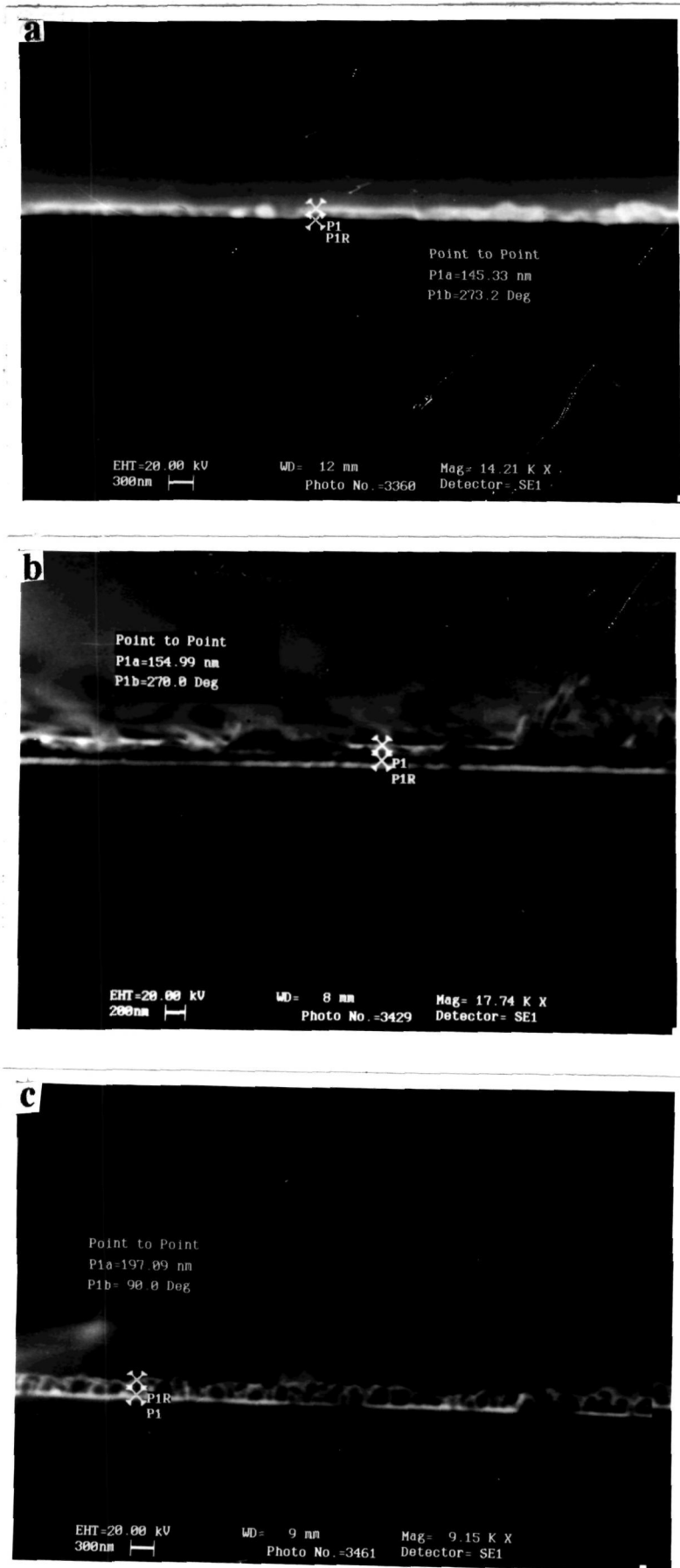


Fig.4.4. Typical cross-sectional SEM images for Cu films deposited at 673K from (a) $\text{Cu}(\text{acac})_2$ (145.33 nm) (b) $\text{Cu}(\text{dpm})_2$ (154.99 nm) and $\text{Cu}(\text{hfac})_2$ (197.09 nm). The thickness of the film is given in the brackets.

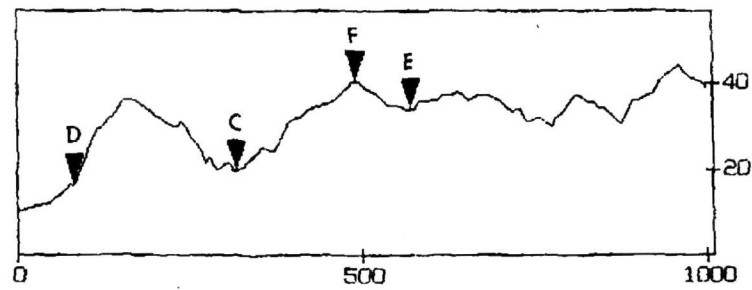
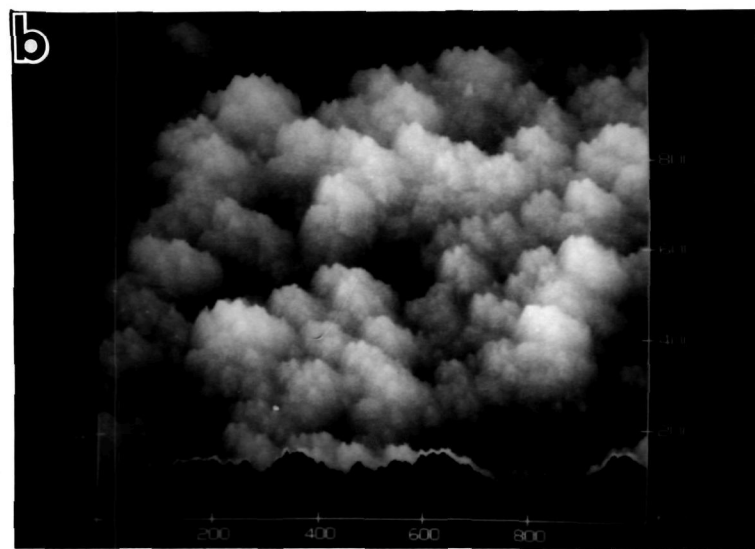
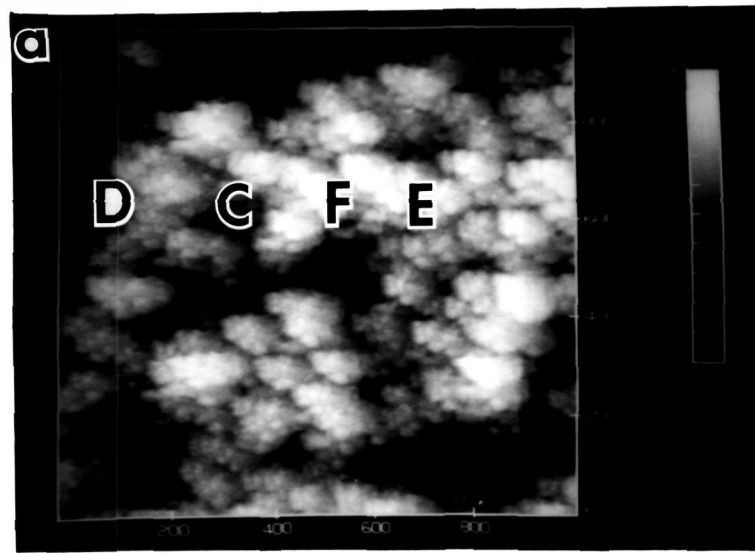


Fig.4.5. STM images of Cu films deposited on Si(100) substrates deposited 673 K $\text{Cu}(\text{dpm})_2$, (a) topview, (b) surface-plot in 60° perspective and (c) line profile taken across 'D-C-F-E' as marked in (a) .

population of 70-80 nm grains. Thus, the observed average grain size increases with the deposition temperature. At deposition temperatures higher than 623 K, the size levels off to ~ 115 nm giving a bimodal grain size distribution. The observed saturation of average grain size at higher temperatures is due to the formation of new small grains at the different nucleation sites.

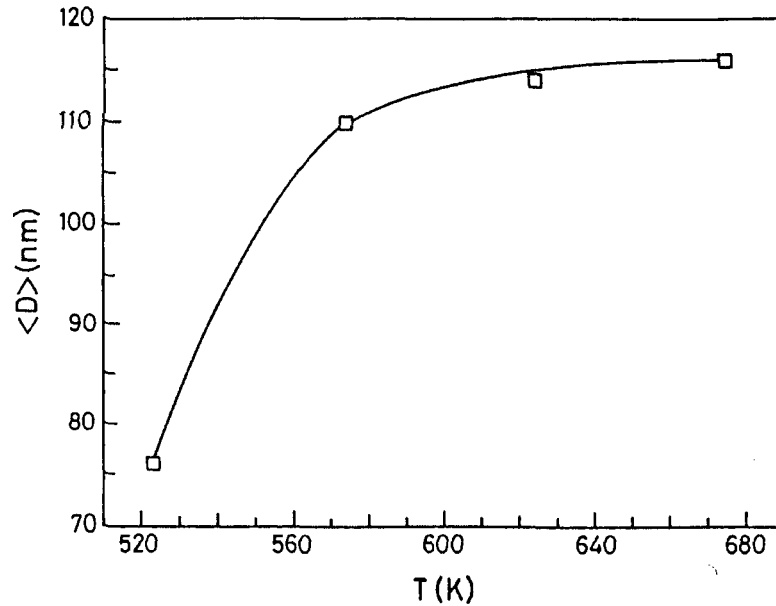


Fig.4.6. Variation of average grain size <D> with deposition temperature for Cu films Deposited from Cu(acac)₂

(c) Growth Aspects: In view of the practical applications of copper films, the rate of film growth is a vitally important parameter. The growth rate, d/t , of copper films from the different Cu precursors was estimated from the knowledge of the film thickness, d , attained in a known length of deposition time, t . We have compared the growth rates for the Cu depositions carried out under the similar experimental conditions such as the substrate temperature (673 K), precursor concentration (~1 mM) and the carrier gas (N₂/H₂) mixture flow rate (1 lit/min). The films from Cu(acac)₂ exhibited the highest growth rate of ~19 Å/min. The growth rate reduced to a low value of 3 Å/min for Cu(hfac)₂. In the case of Cu(dpm)₂, an intermediate growth rate of 14 Å/min was observed. The cause for such differences in the growth rate of the films obtained from the different precursors is not clear

at present. It is possible that the structure of the precursor molecule has some influence on the growth rate since bond breaking is essential before the metal film is deposited. It should be noted that the growth rates observed by us are smaller than the deposition rates of 200 to 400 Å/min required in real situations. In nebulized spray pyrolysis, the growth rate is determined by the concentration of the precursor, nebulized spray flow rate, carrier gas flow rate and the substrate temperature⁸. It should be possible to optimize these parameters to achieve higher growth rates.

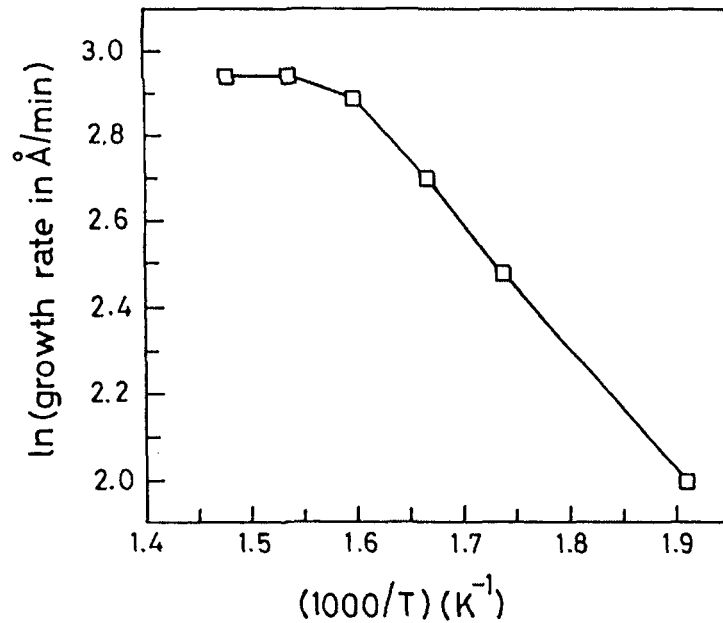


Fig.4.7. Arrhenius plot of growth rate versus deposition temperature of copper films deposited from $\text{Cu}(\text{acac})_2$ on Si (100) substrates by nebulized spray pyrolysis

Fig.4.7 shows the Arrhenius plot of the growth rate of the films deposited on Si(100) substrate using the $\text{Cu}(\text{acac})_2$ precursor over the 523-673 K range. There is a linear relation over the most part of the temperature range, indicating thermally activated deposition kinetics. Around 650 K, the growth rate becomes nearly independent of the substrate temperature, suggesting the onset of diffusion-controlled growth. The activation energy, E_a , estimated from the linear segment of this plot using Arrhenius relation

$$G = A \text{Exp}(-E_a/RT) \quad (1)$$

turns out to be ~ 90 kJ/mol. This value is comparable to the previously reported values of the activation energies for copper film growth by MOCVD^{39,40}.

(d) Transport properties: The temperature dependence of the electrical resistivity of the films from $\text{Cu}(\text{acac})_2$, $\text{Cu}(\text{hfac})_2$ and $\text{Cu}(\text{dpm})_2$ deposited under the similar deposition conditions (at 673 K) is presented in Fig.4.8.

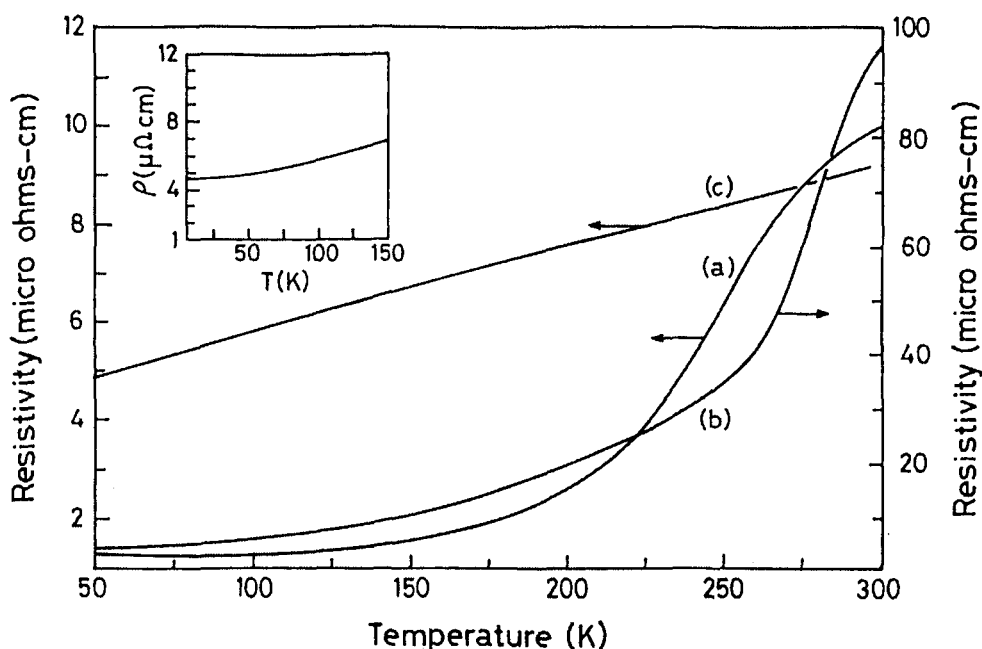


Fig.4.8. Variation of resistivity with temperature for copper films at 673 K from (a) $\text{Cu}(\text{acac})_2$ (b) $\text{Cu}(\text{hfac})_2$ (c) $\text{Cu}(\text{dpm})_2$. Inset shows data (up to 4.2 K) of Cu films from $\text{Cu}(\text{dpm})_2$

All the films show metallic conduction in the 300K-50K range. The room temperature resistivity value is lowest ($9.3 \mu\Omega\text{cm}$) for the films deposited from $\text{Cu}(\text{dpm})_2$. This is close to the Cu films deposited by low pressure MOCVD³⁸, but higher than the $1.67 \mu\Omega\text{cm}$ value of bulk copper. The resistivity of the films from $\text{Cu}(\text{hfac})_2$ is nearly two orders of magnitude larger than that for the films from $\text{Cu}(\text{dpm})_2$ or $\text{Cu}(\text{acac})_2$. On the basis of the structural and morphological aspects of the films deposited from the three precursors, it is possible to relate the resistivity behavior to the crystallinity and the microstructure. Thus, the high resistivity of the Cu films derived from $\text{Cu}(\text{hfac})_2$ is likely to be due to the poor

intergrain connectivity and the porous microstructure. On the other hand, the dense, fine-grained and smooth morphology of the films from $\text{Cu}(\text{dpm})_2$ and $\text{Cu}(\text{acac})_2$ yielded significantly lower resistivities.

The mean free path of the conduction electrons is an important quantity in determining the electrical conductivity of metals. Its value depends on the degree of perturbation of the crystalline lattice by the thermal motion of the lattice and the structural defects. The mean free path, l , of the electrons in the Cu films discussed here was obtained using the Drude relation:

$$l = \frac{mv_f}{n_e e^2 \rho} \quad (2)$$

where e is the electronic charge, m its mass, n_e is the electron density in pure bulk copper ($8.47 \times 10^{22} / \text{cm}^3$), v_f is the fermi velocity of electrons in copper ($1.57 \times 10^8 \text{ cm/s}$) and ρ is the observed resistivity. The different electrical characteristics including the mean free paths of the films are listed in table I. The films derived from different precursors exhibit a positive temperature coefficient of resistivity (TCR). The TCR was obtained using equation

$$\text{TCR} = (1/\rho_1)[(\rho_2 - \rho_1)/(T_2 - T_1)] \quad (3)$$

Here, ρ_1 and ρ_2 are the resistivities of the film at temperatures T_1 and T_2 respectively. The TCR value for pure copper metal is 2.91 K^{-1} , for bulk copper wire it is 0.0907 K^{-1} and for copper films obtained from $\text{Cu}(\text{dpm})_2$, it is 3.4×10^{-3} (at $T_1 = 4.2 \text{ K}$, $T_2 = 300 \text{ K}$)¹⁵. The TCR values obtained for the films from all the three precursors is presented in Table 1. Although the films deposited from $\text{Cu}(\text{hfac})_2$ show porous morphology with a void structure, it is not a discontinuous film as reflected in its positive TCR value. For discontinuous films with islands, negative TCR is generally observed³⁸.

Table I

Sample	$\rho_{(50K)}$ $\mu \Omega\text{cm}$	$\rho_{(300K)}$ $\mu \Omega\text{cm}$	$l_{(50K)}$ nm	$l_{(300K)}$ nm	TCR_{obs} (300K-50K)
Cu/Si(100)fromCu(acac) ₂	1.3	10.7	49	6	2.8×10^{-2}
Cu/Si(100) fromCu(hfac) ₂	9.3	98.5	7	1	3.8×10^{-2}
Cu/Si(100) from Cu(dpm) ₂	4.9	9.3	14	7	3.6×10^{-3}
Cu/Si(100) from Cu(dpm) ₂	4.65 ($\rho_{4.2K}$)	9.3	14	7	3.4×10^{-3} (300K-4.2K)
Cu wire	0.06 ($\rho_{4.2K}$)	1.67	1098	39.7	9.07×10^{-2} (300K-4.2K)

The residual resistivity ratio (RRR) defined as the ratio of the resistivity at 300 K to that at 4.2 K (i.e. $\rho_{300\text{ K}}/\rho_{4.2\text{ K}}$), is taken to be a direct measure of the quality of the metal films. We have carried out the low temperature measurements down to 4.2 K for the films from Cu(dpm)₂ which showed the best resistivity behavior in this work (see inset of Fig.4.8.). The RRR value for these films is 2, which compares well with the value for the films obtained from MOCVD³⁸. Pure copper exhibits a RRR of 862.5 (calculated using resistivity values taken from CRC Handbook of Chemistry and Physics, 78th Edition, 1997-98) and for copper wire, it is 27.8. Copper films exhibiting near bulk resistivities and high RRR value have been deposited by PVD methods^{41,42}.

According to Matthiessen's rule, the resistivity of metals can be considered to be sum of a residual non-thermal component, ρ_0 , and a thermal component, ρ_T :

$$\text{i.e., } \rho_{\text{total}} = (\rho_0 + \rho_T) \quad (4)$$

Assuming $\rho_{4.2\text{ K}} \approx \rho_0$, the temperature dependent part of resistivity of the Cu films from Cu(dpm)₂ is 4.65 $\mu\Omega\text{-cm}$. For bulk copper wire, this contribution is $\sim 1.61 \mu\Omega\text{-cm}$, which arises only from electron-phonon interaction. The deviation from Matthiessen's rule possibly arises from enhanced electron-phonon interactions. The high resistivity of the films compared to bulk copper can arise from (i) grain-boundary scattering (ii) surface scattering (iii) defect

scattering and (iv) impurity scattering. Typical contributions to the resistivity from the plane defects are reported to be $\sim 3.1 \times 10^{-8} \mu \Omega\text{-cm}$ per stacking fault and $\sim 1 \times 10^{-7} \mu \Omega\text{-cm}$ per twin^{43,44}. As the densities of such defects in the polycrystalline metal films are of the order of 10^5 per cm^3 or less, these together have little effect on the observed resistivity⁴⁵. Vacancies also do not influence the resistivity in a discernible manner, with a typical vacancy density of $\sim 10^{-8}$ at 300 K⁴⁶.

The Cu films deposited from $\text{Cu}(\text{dpm})_2$ are polycrystalline although there is high preferred (111) orientation. These contain grains of ~ 40 nm as observed in the STM images. The extent to which the resistivity is increased by grain-boundary scattering depends on the average grain size and the quality of the film. On the basis of the Mayadas-Shatzkes (MS) grain-boundary scattering model⁴⁷, the resistivity data can be analyzed by considering the influence of only the grain-boundary scattering on the excess of resistivity, assuming the Fuch's specularity parameter, $p=1$ ⁴⁸. The grain boundary enhanced resistivity is given by:

$$\rho_{\text{gr}}(T) = [\rho(T) / f(\alpha)] \quad (5)$$

$$\text{where, } f(\alpha) = [1 - (3/2)\alpha + 3\alpha^2 - 3\alpha^3 \ln\{1 + (1/\alpha)\}] \quad (6)$$

$$\text{and } \alpha = [l(T) / \langle D \rangle \{R / (1-R)\}] \quad (7)$$

$$\rho_F = [(1/\rho_{\text{gr}}) - \{(1/\rho_0) * A\}]^{-1} \quad (8)$$

$$\text{with } A = (6 / \pi * k)(1-p) \int_0^{\pi/2} d\phi \int_1^{\infty} \{\cos^2 \phi / H^2(t, \phi)\} \{(1/t^3) - (1/t^5)\} \{[1 - \exp\{-ktH(t, \phi)\}] / [1 - \exp\{-ktH(t, \phi)\}]\} dt$$

where p is the probability that an electron will be specularly reflected upon scattering from the film surface, k is the reduced film thickness (the film thickness a divided by the electron mean free path l_0), t and ϕ are integration variables and the function $H(t, \phi)$ is defined by

$$H(t, \phi) = 1 + \alpha \cos^{-1} \phi (1-t^{-2})^{-1/2} \quad (9)$$

Hence

$$(\rho_F / \rho_{\text{gr}}) = \{1 - (A/f(\alpha))\}^{-1} \quad (10)$$

and $(\rho_F / \rho_\infty) = \{f(\alpha) - A\}^{-1}$ (11)

In the above equations, $\rho_\infty(T)$ is the total resistivity of the pure bulk material at temperature T, $\langle D \rangle$ is the average grain diameter in the film, R is the reflection coefficient of electrons striking the grain boundaries ($0 \leq R \leq 1$). $l_\infty(T)$ is the mean free path of the bulk material at temperature T without the grain boundaries.

By using the limiting form of equation (6) for $\alpha \leq 1$, $f(\alpha) = (1 + 3/2 \alpha)$, the equation (5) can be written as

$$\rho_{gr}(T) = \rho_\infty(T) / [1 + \{(3/2)l_\infty(T)/\langle D \rangle\} \{R/(1-R)\}] \quad (12)$$

where $\rho_\infty(T)$ is the resistivity of pure copper metal at temperature (T) and $\langle D \rangle$ (= 40nm) is the average grain size of copper film obtained from Cu(dpm)_2 . Equation (12) can be written as

$$\rho_{gr}(T)\langle D \rangle = \rho_\infty(T)\langle D \rangle + [(3/2)l_\infty(T)]\{R/(1-R)\} \quad (13)$$

If 'd' is the thickness of the film and multiplying (13) by 'd/⟨D⟩' we get,

$$\rho_{gr}(T)(d) = \rho_\infty(T)(d) + [(3/2)l_\infty(T).\rho_\infty(T)]\{R/(1-R)\} (d)/\langle D \rangle \quad (14)$$

In the above equation, the term $[(3/2)l_\infty(T).\rho_\infty(T)]\{R/(1-R)\}(d)/\langle D \rangle$ is the size effect induced grain boundary scattering. This value can be obtained from the plot of $\rho_{gr}(T)(d)$ verses (d) for different film thicknesses. The values of resistivities for films of 100, 125 and 155 nm thickness are 10.2, 9.8 and 9.3 $\mu\Omega\text{cm}$ respectively for films obtained from Cu(dpm)_2 . This plot gave the Y intercept as $0.26 \times 10^{-6} \mu\Omega\text{cm}$ and slope as $7.63 \mu\Omega \text{ cm}$. We have estimated the reflection coefficient, R as 0.398. The value of $l_\infty(T)$ is calculated from the knowledge of $(\rho l)_\infty$ and $\rho_\infty(T)$. The product $(\rho l)_\infty$ is assumed to have a constant value of $6.6 \times 10^{-12} \Omega \text{ cm}^2$ for bulk copper^{38,47}. The values of α and $f(\alpha)$ are calculated from the equations (6) and (7) and are 0.142 and 0.829 respectively. The grain boundary resistivity ρ_{gr} is estimated from the equation (5) as $2.08 \mu\Omega \text{ cm}$ (by taking the ρ_∞ at 300 K for pure copper metal as $1.725 \mu\Omega \text{ cm}$).

The reported values of R range between 0.4-0.8 for Cu films obtained by the MOCVD technique³⁸. A reflection coefficient of ~ 0.35 has been reported by Sambles et al⁴⁹ for (111) oriented Au films deposited by the PVD method. It appears that the more dense, smooth and preferentially (111) oriented microstructure of the Cu film deposited from $\text{Cu}(\text{dpm})_2$ gives a low R value. We have not attempted to estimate exactly the surface scattering contribution to resistivity. There seems to be a definite contribution due to this mechanism as the film shows deviation from Matthiessen's rule. In the light of the above discussion, the high resistivity of Cu film from $\text{Cu}(\text{dpm})_2$, relative to bulk Cu arises from the combined effect of surface scattering and impurity scattering. We believe that the impurity scattering term could be significant as the RRR observed for this film is quite low (~ 2). We have however not estimated the impurity scattering contribution.

The ambient stability of the Cu films deposited from different precursors was evaluated by studying the changes in their room temperature resistivity ($\rho_{300\text{K}}$) with the duration of film exposure to the ambient atmosphere. The maximum duration of exposure was 72 hours. The results are shown in Fig.4.9 where the solid lines shown are the best fits of the observed data

$$\log(\rho_f) = [A + B t] \quad (15)$$

From Fig.4.9, we see that all the films exhibit a linear increase in the logarithm of resistivity with the duration of exposure. The slope of such a plot can be taken as the rate of degradation of these films i.e., the fit parameter B can be treated as a rate constant to compare the relative stability of the films. Accordingly, the rate constants for the films from $\text{Cu}(\text{acac})_2$, $\text{Cu}(\text{hfac})_2$ and $\text{Cu}(\text{dpm})_2$ on Si(100) substrates are 0.011, 0.016 and 0.007 sec^{-1} respectively. The films from $\text{Cu}(\text{hfac})_2$ show fastest degradation in contrast to those deposited from $\text{Cu}(\text{acac})_2$ and

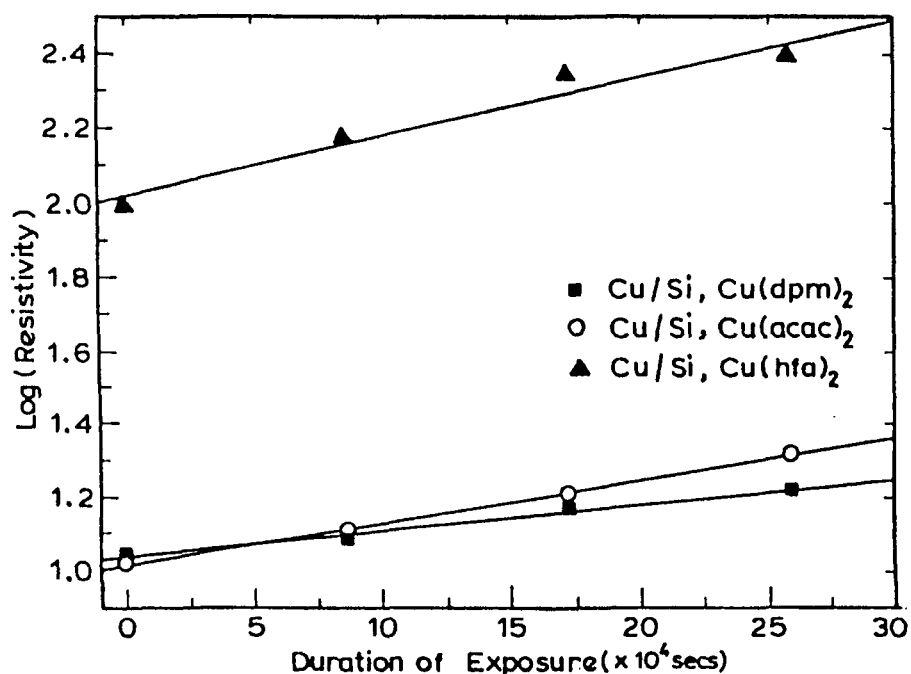


Fig.4.9. Variation of resistivity of as deposited Cu films at 673 K with duration of exposure in air

Cu(dpm)₂. The films from Cu(dpm)₂ appear most stable for the range of exposure compared here, their rate constants being an order of magnitude different. The observed degradation is most likely due to the slow oxidation of the film. It is likely that the presence of adsorbed contaminants and humidity from the ambient would affect the resistivity. It is noteworthy that the Cu films from Cu(hfac)₂ with a void structure and a porous surface morphology show the highest degradation.

4.2. Cobalt and Copper-Cobalt granular alloy films

(a) Cobalt Films

X-ray diffraction studies: The x-ray diffraction patterns of the Co films deposited from Co(acac)₂ on Si(100) and borosilicate glass at 598 K and 673 K are shown in Fig.4.10. The XRD patterns are showing a polycrystalline nature with no indication of an oxide phase. The films deposited on Si(100) show a mixed fcc and hcp phase at 598 K but a fcc phase only at 673 K. On the other hand films deposited in borosilicate glass showed a mixed fcc and hcp phases both the temperatures.

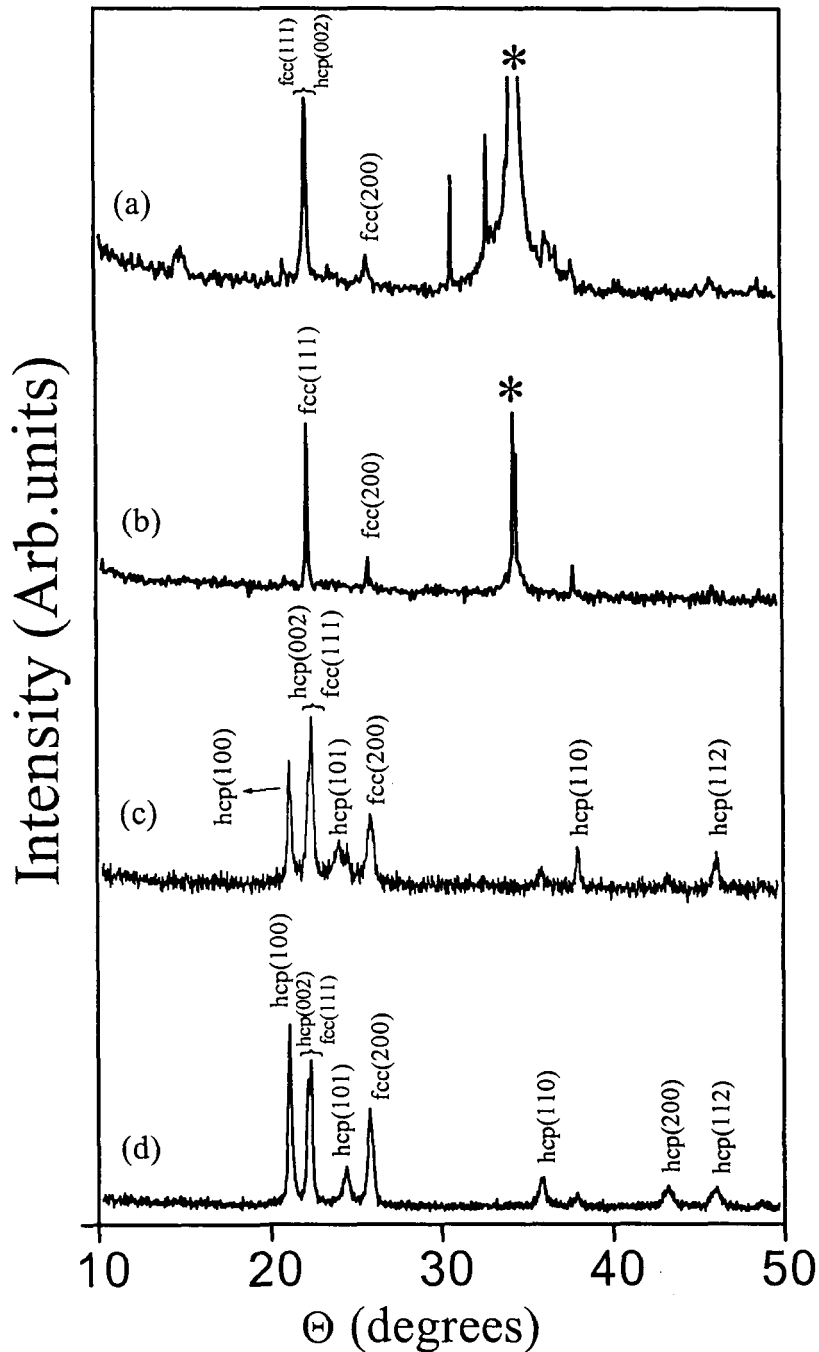


Fig.4.10. The X-ray diffraction patterns of Co films deposited on Si(100) substrates at (a) 598 K (b) 673 K and on glass substrate at (c) Si(100) and (d) 673 K. * denotes Si(100) reflection.

Morphology: In order to conform the mixture of phases obtained at different temperatures SEM was done on the films. Fig.4.11(a) and (b) shows SEM images of the films deposited on Si(100) and Fig.4.11(c) and (d) on borosilicate glass at 598 K and 673 K respectively. The films deposited on Si(100) at 598 K clearly reveal a needle shaped flaky morphology and

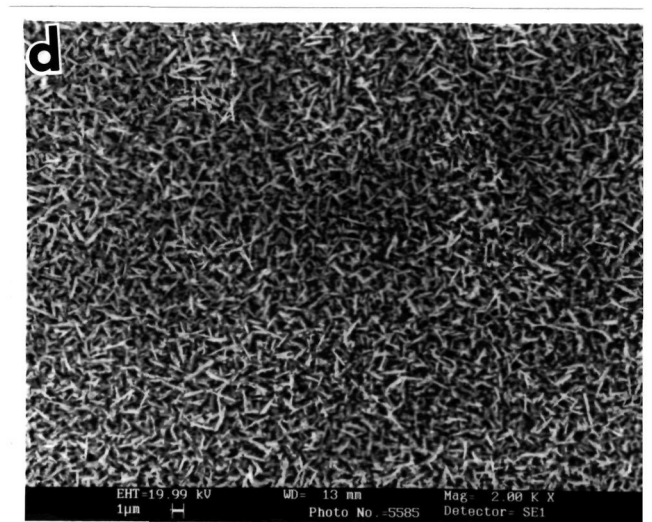
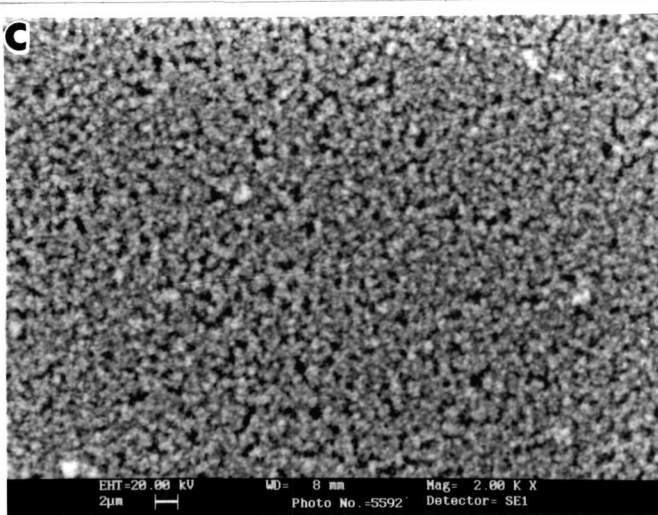
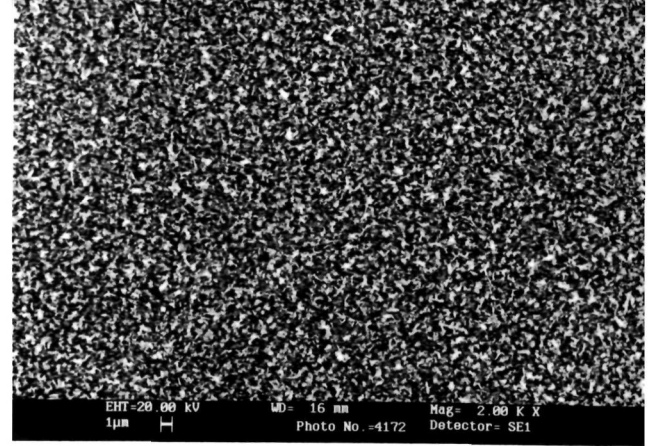
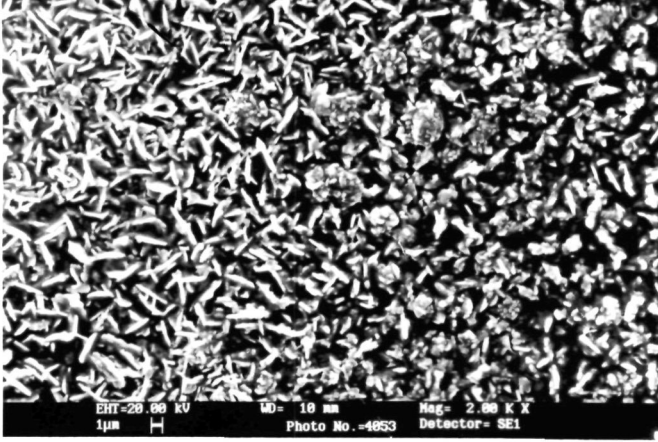


Fig. 4.11. Scanning electron micrographs of Co films on Si (100) substrate at temperature (a) 598 K and (b) 673 K and on glass substrate at temperature (c) 598 K and (d) 673 K.

granular morphology was observed for the films deposited at 673 K. The films deposited on glass show a granular and needle shaped flaky-type morphology at 598 K and 673 K respectively.

Electrical Transport Properties: Electrical resistivity data of the Co films on the Si(100) and on glass substrates deposited at 673 K are shown in Figs. 4.12 (a) and (b) respectively. The data clearly reveal the expected metallic behavior. The values of resistivity of the Co films on the Si(100).

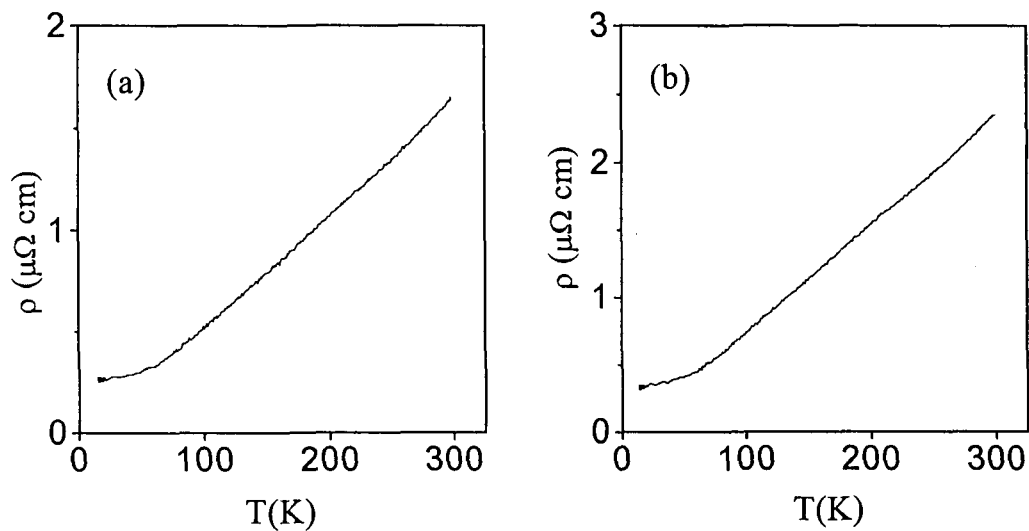


Fig.4.12. Electrical resistivity of Co films deposited at 673K on (a) Si(100) (b) Glass

substrate at 300 K and 15 K are 1.646 $\mu\Omega$ cm and 0.258 $\mu\Omega$ cm respectively. The resistivity values of the films on the glass substrate are 2.347 $\mu\Omega$ cm and 0.327 $\mu\Omega$ cm at 300 K and 15 K respectively. The resistivity of the films on the glass substrate is somewhat higher probably because of the presence of mixed phases of Co. This low resistivity of the films is due to single fcc phase present on Si(100).

Magnetic properties: Magnetic hysteresis loop measurements of the Co films on Si(100) and on glass substrates were recorded with the magnetic field parallel and perpendicular to the film. The results are shown in Fig. 4.13. The films deposited at 598 K gave good square

loops when field is parallel to the film surface. The loops are not as good in the perpendicular direction as generally expected in films. The saturation magnetization values for the films

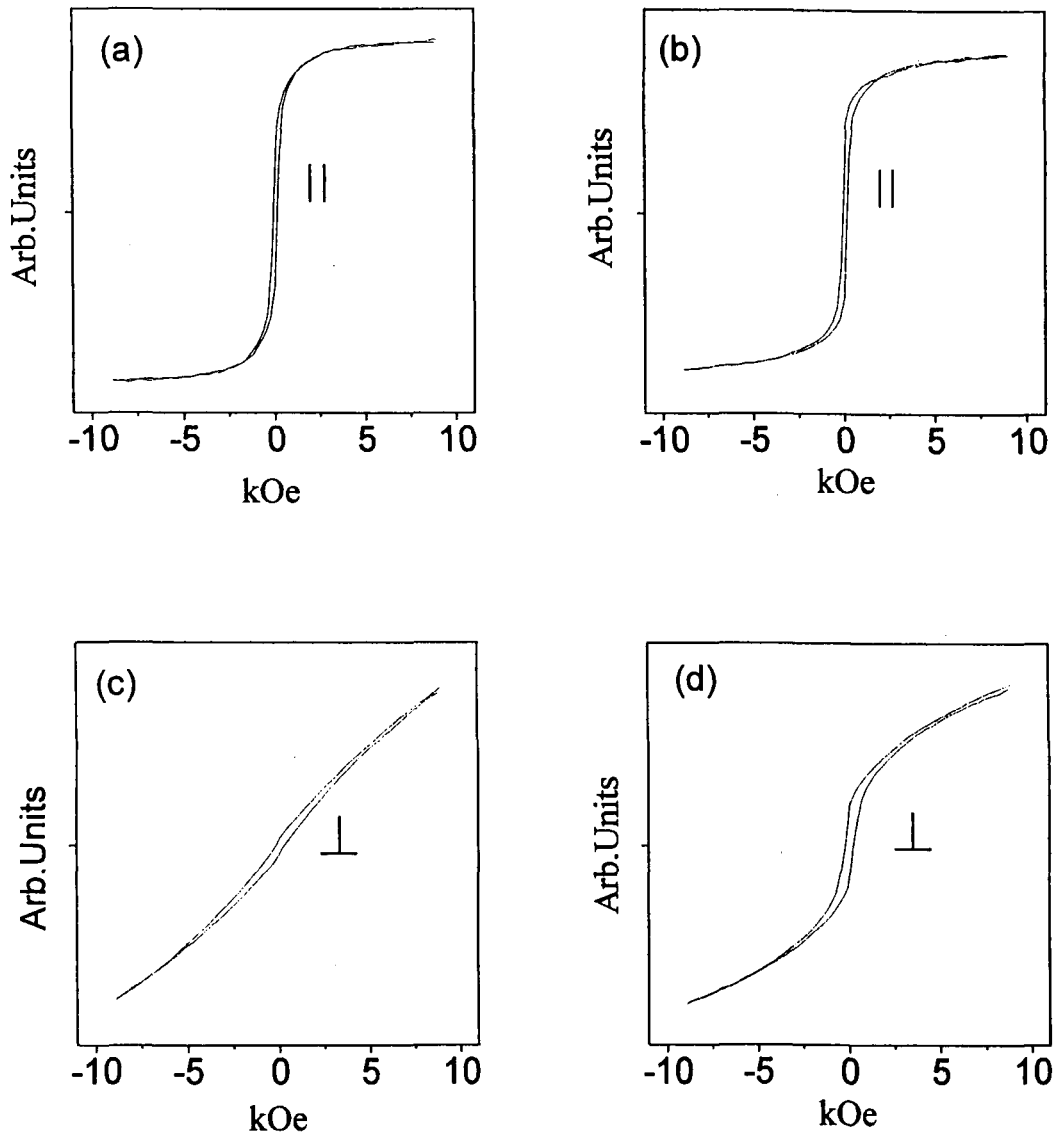


Fig.4.13. Magnetic hysteresis loops of Co films deposited at 598K on Si(100) with field (a) parallel and (c)perpendicular; and on glass substrate with field (b) parallel and (d) perpendicular to the surface

deposited on Si(100) at 598 K are 30 emu/g and 21 emu/g in the parallel and perpendicular directions respectively. For the films deposited on glass substrates, the saturation

magnetization values are 65 emu/g and 53 emu/g respectively in the parallel and perpendicular directions.

(b) Granular Cu-Co alloy films

X-ray diffraction studies: In Fig. 4.14(a) we show the x-ray diffraction pattern of the as-deposited films of $\text{Cu}_{82}\text{Co}_{18}$ at 673 K. On annealing the film in hydrogen at 923 K, we notice phase separation in the $\text{Cu}_{82}\text{Co}_{18}$ film as can be seen from the XRD pattern in Fig. 4.14(b). In the case of the $\text{Cu}_{50}\text{Co}_{50}$ composition, there is phase separation in the as-deposited film (at 673 K) as can be seen in Fig.4.14c.

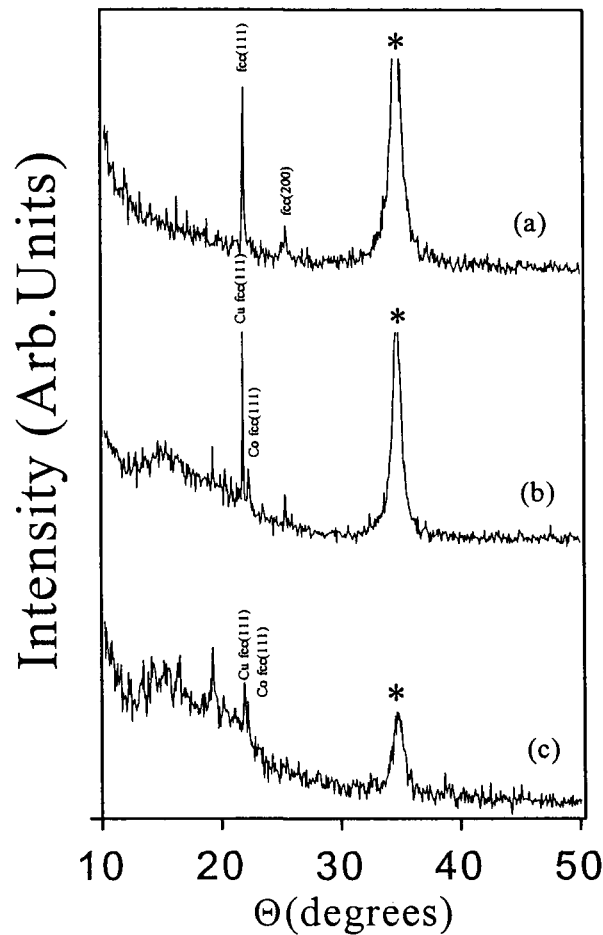


Fig.4.14. X-ray diffraction patterns of Cu-Co granular films deposited at 673 K (a) as-deposited and (b) hydrogen annealed at 923 K for the films of $\text{Cu}_{82}\text{Co}_{18}$ and (c) as-deposited film of $\text{Cu}_{50}\text{Co}_{50}$. '*' denotes Si(100) reflection.

Such phase separation on annealing $\text{Cu}_{82}\text{Co}_{18}$ is known in the literature¹⁸.

Magnetic properties: Magnetic hysteresis loop measurements were carried out on the $\text{Cu}_{82}\text{Co}_{18}$ and $\text{Cu}_{50}\text{Co}_{50}$ films. In Fig. 4.15, we show typical hysteresis loops obtained with the $\text{Cu}_{50}\text{Co}_{50}$ film deposited on Si(100) at 673 K. The loops obtained with the field parallel and perpendicular to the film are both shown in the figure. In the parallel orientation, good square loops are obtained. The magnetization values for the $\text{Cu}_{50}\text{Co}_{50}$ film deposited at 673 K are 29 emu/g and 28.5 emu/g respectively with the field parallel and perpendicular to the film surface.

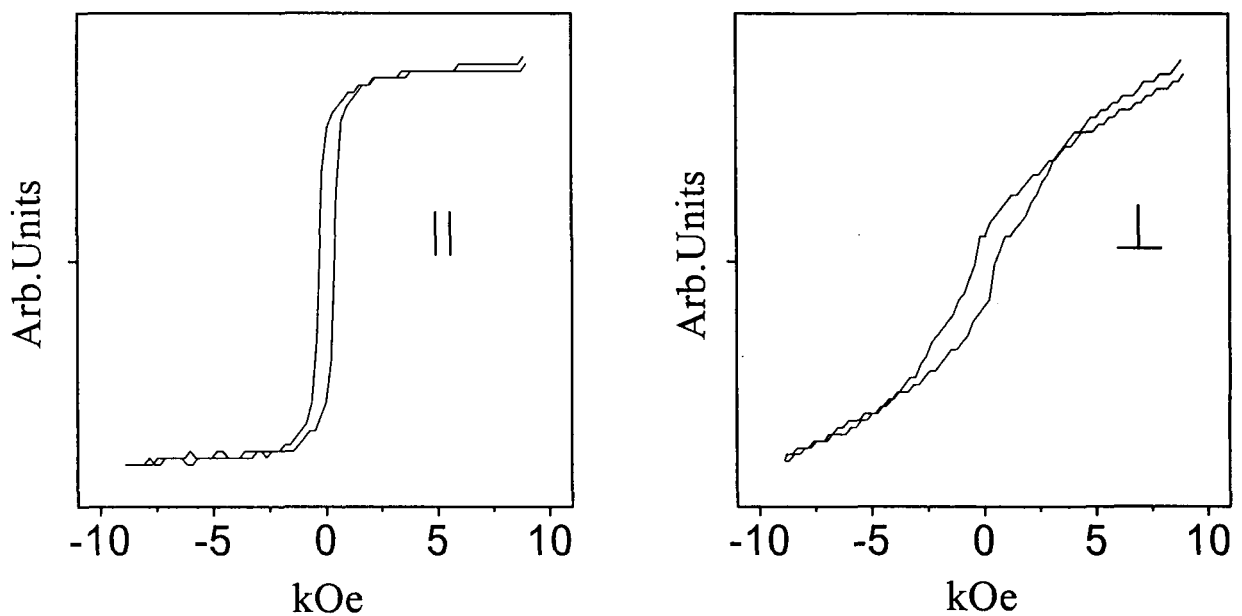


Fig.4.15. Magnetic hysteresis loops of $\text{Cu}_{50}\text{Co}_{50}$ film deposited at 673 K on Si(100) with field (a) parallel and (b) perpendicular to the surface of the film.

Magnetoresistance measurement: Magnetoresistance (MR) measurements were carried out on both the $\text{Cu}_{50}\text{Co}_{50}$ and $\text{Co}_{18}\text{Cu}_{82}$ films. The results are presented in Fig.4.16. We have obtained MR of 0.28 % and 0.14% respectively for the $\text{Cu}_{50}\text{Co}_{50}$ and $\text{Cu}_{82}\text{Co}_{18}$ films at a field of 1.2 kOe at 300 K. This is quite satisfactory, considering that other workers have obtained around 3% MR at a field of 5 tesla or higher^{19,20}.

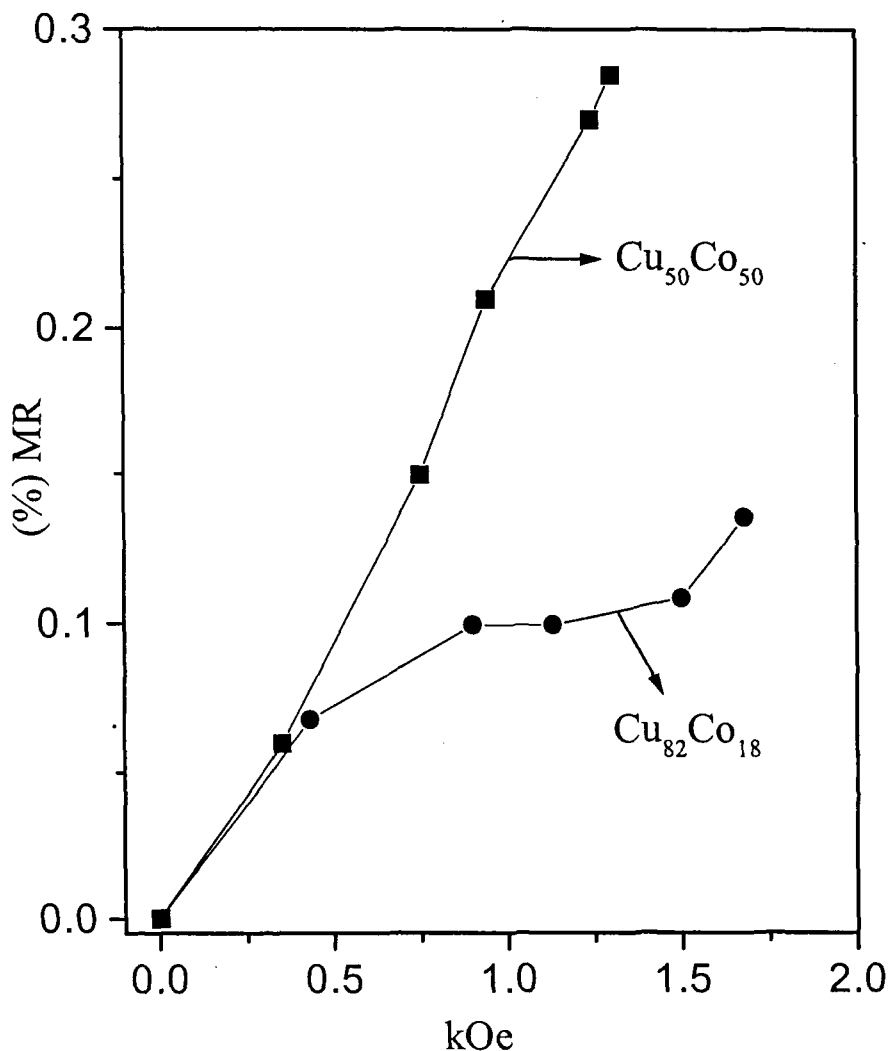


Fig.4.16. Field dependence of the magnetoresistance of the $\text{Cu}_{50}\text{Co}_{50}$ and $\text{Cu}_{82}\text{Co}_{18}$ films deposited at 673 K on Si(100)

4.3. Films of charge-ordered rare earth manganates

Thin films of charge-ordered rare earth manganates^{22,23} of the formulae $\text{Nd}_{0.5}\text{Ca}_{0.5}\text{MnO}_3$ (NCM), $\text{Gd}_{0.5}\text{Ca}_{0.5}\text{MnO}_3$ (GCM), $\text{Y}_{0.5}\text{Ca}_{0.5}\text{MnO}_3$ (YCM) and $\text{Nd}_{0.5}\text{Sr}_{0.5}\text{MnO}_3$ (NSM) were deposited on Si(100) and $\text{LaAlO}_3(100)$ by employing nebulized spray pyrolysis. Since this technique involves the deposition of precursor solutions at relatively low temperatures, sufficient control could be achieved on the stoichiometry of the films.

(a) **X-ray diffraction studies:** The films of the manganates had a polycrystalline nature on the Si(100) substrate, but were oriented in the (100) direction on $\text{LaO}(100)$ substrate. Fig.4.17 shows the x-ray diffraction patterns of the films of $\text{Nd}_{0.5}\text{Ca}_{0.5}\text{MnO}_3$, $\text{Gd}_{0.5}\text{Ca}_{0.5}\text{MnO}_3$ and $\text{Y}_{0.5}\text{Ca}_{0.5}\text{MnO}_3$ on Si(100).

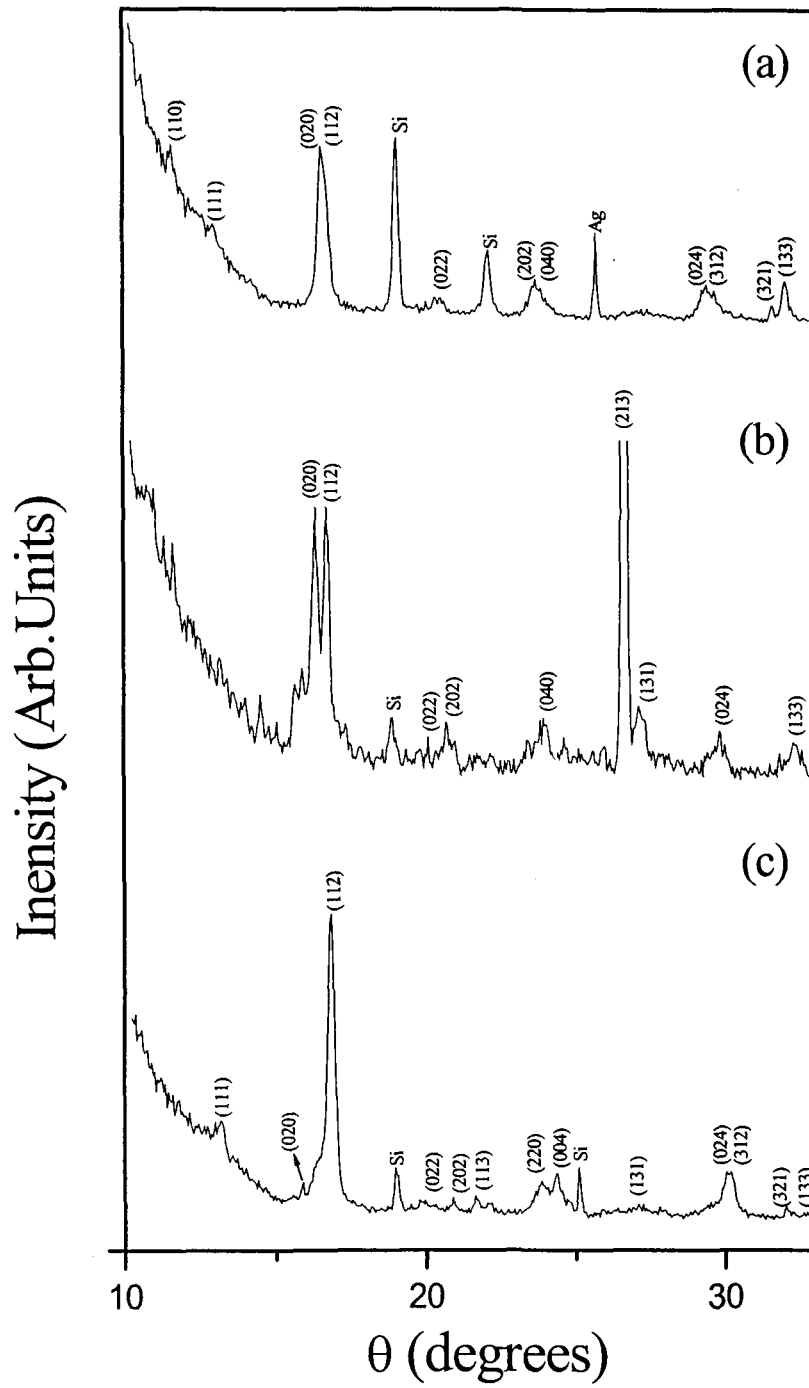


Fig.4.17. X-ray diffraction patterns of films of (a) $\text{Nd}_{0.5}\text{Ca}_{0.5}\text{MnO}_3$
 (b) $\text{Gd}_{0.5}\text{Ca}_{0.5}\text{MnO}_3$ (c) $\text{Y}_{0.5}\text{Ca}_{0.5}\text{MnO}_3$ on Si(100)

Fig.4.18 shows the x-ray diffraction patterns of the films on LAO(100) substrate. In the patterns we see only three reflections i.e. (100), (200) and (300) of the substrate LAO(100) and of the manganates. The reflections due to manganates are weaker than those of the substrate.

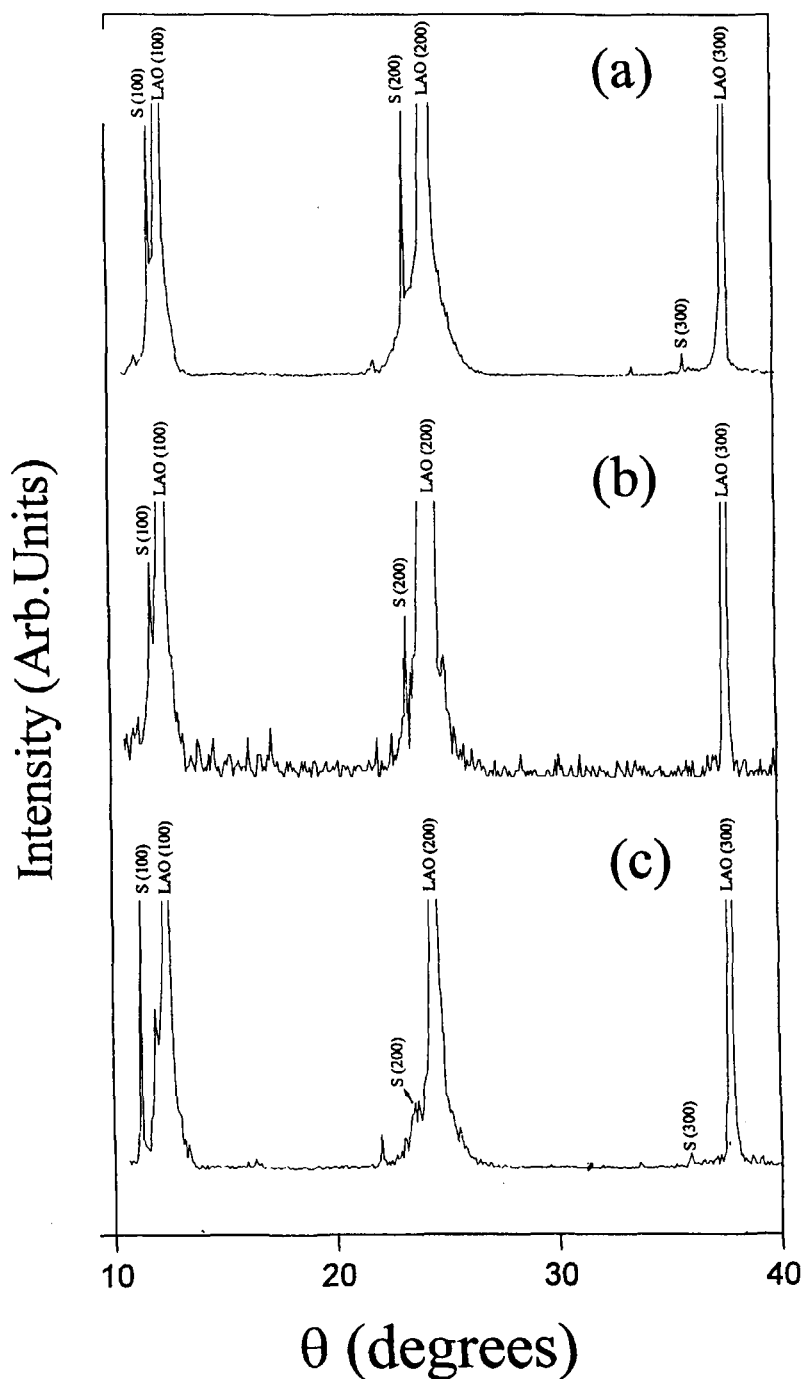


Fig.4.18 X-ray diffraction patterns of films of (a) $Nd_{0.5}Ca_{0.5}MnO_3$ (b) $Gd_{0.5}Ca_{0.5}MnO_3$ (c) $Y_{0.5}Ca_{0.5}MnO$ on LAO(100) 'S' denotes reflections due to the rare earth manganate

The orientation on LAO(100) was achieved due to close matching of the lattice parameters of both the film material and the substrate. Due to the oriented nature of the manganate films on LAO(100), the electrical resistivity was considerably higher than on the Si(100) substrate.

(b) Electrical transport properties: The electrical resistivity of the films was studied by the four-probe method over the temperature range from 300 to 15 K using a closed cycle refrigerator. In Fig.4.19 we show the temperature variation of resistance of a polycrystalline

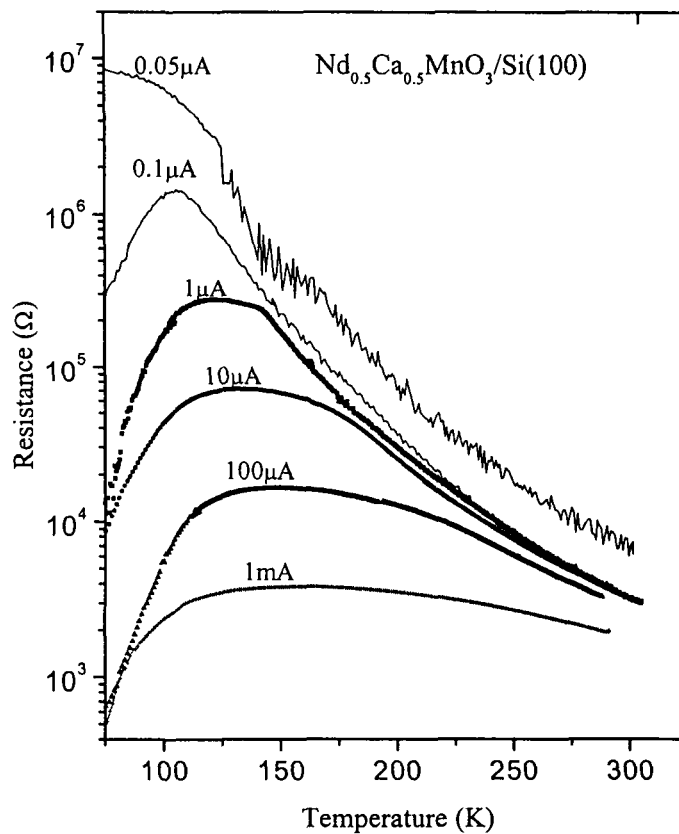


Fig.4.19 Temperature variation of the resistance of a polycrystalline $Nd_{0.5}Ca_{0.5}MnO_3$ film deposited on Si(100) for different current values

deposited on Si(100), for different values of the d.c current passed. With a current of 0.05 μA , the film shows the known insulating behavior of NCM. With increasing current, however, we see the definitive occurrence of an insulator-metal (I-M) transition. It is noteworthy that even a current of 0.1 μA causes the I-M transition. it was ascertained that the

observed effects were not to be due to local heating. Local heating effects become apparent only at higher current values (≥ 50 mA). The temperature of the I-M transition shifts from 100 to 150 K with increase in current. Measurements on the highly oriented NCM film deposited on LAO also shows the negative differential resistance (Fig.4.20), with the resistance decreasing markedly with increasing current. We do not clearly see a metal-like decrease in resistance at low temperatures, and the behavior is similar to that in the I-M transition of laser-irradiated $\text{Pr}_{1-x}\text{Ca}_x\text{MnO}_3$ crystals reported by Ogawa et al²⁷.

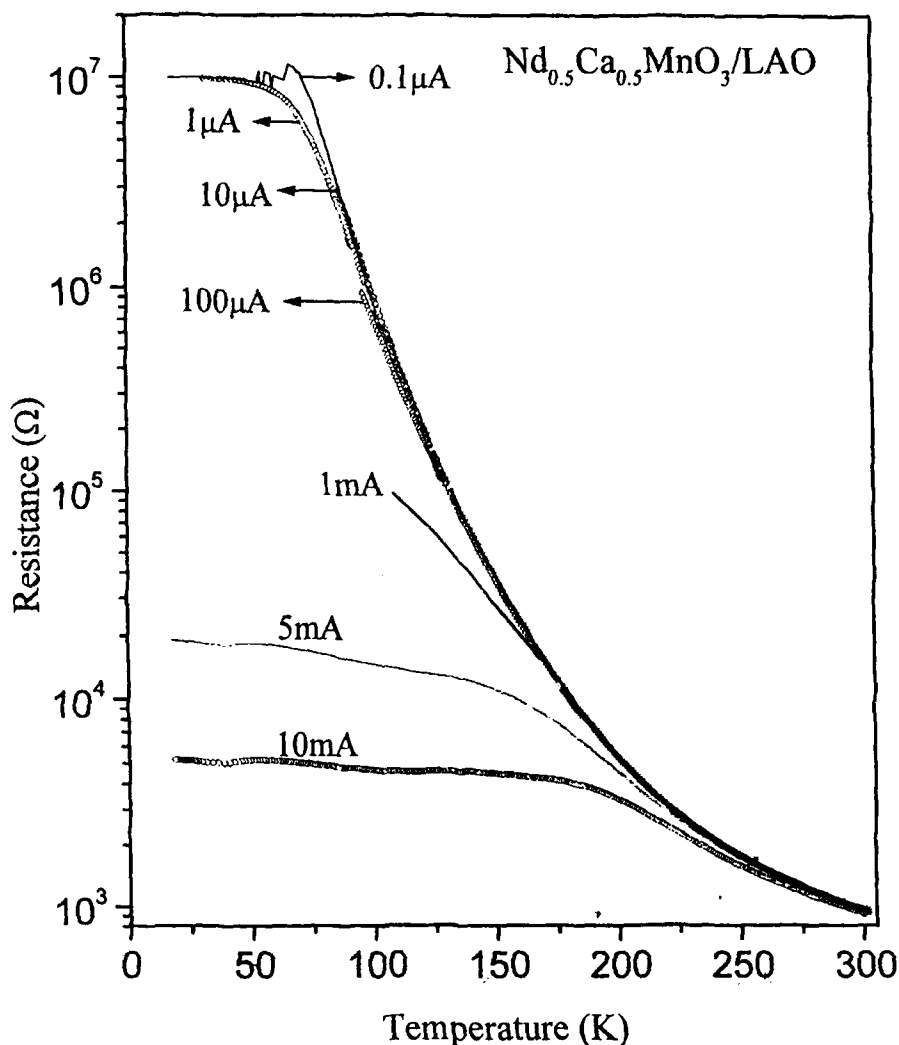


Fig.4.20 Temperature variation of the resistance of an oriented $\text{Nd}_{0.5}\text{Ca}_{0.5}\text{MnO}_3$ film deposited on LAO(100) for different values of current

In case of the polycrystalline films of $Gd_{0.5}Ca_{0.5}MnO_3$ on Si(100) we did not see a clear I-M transition but could see a clear melting of charge-ordered state. The current induced negative differential resistance (NDR) is clearly visible here also. Fig. 4.21 shows the temperature dependence of the resistance for the film of $Gd_{0.5}Ca_{0.5}MnO_3$ on Si(100).

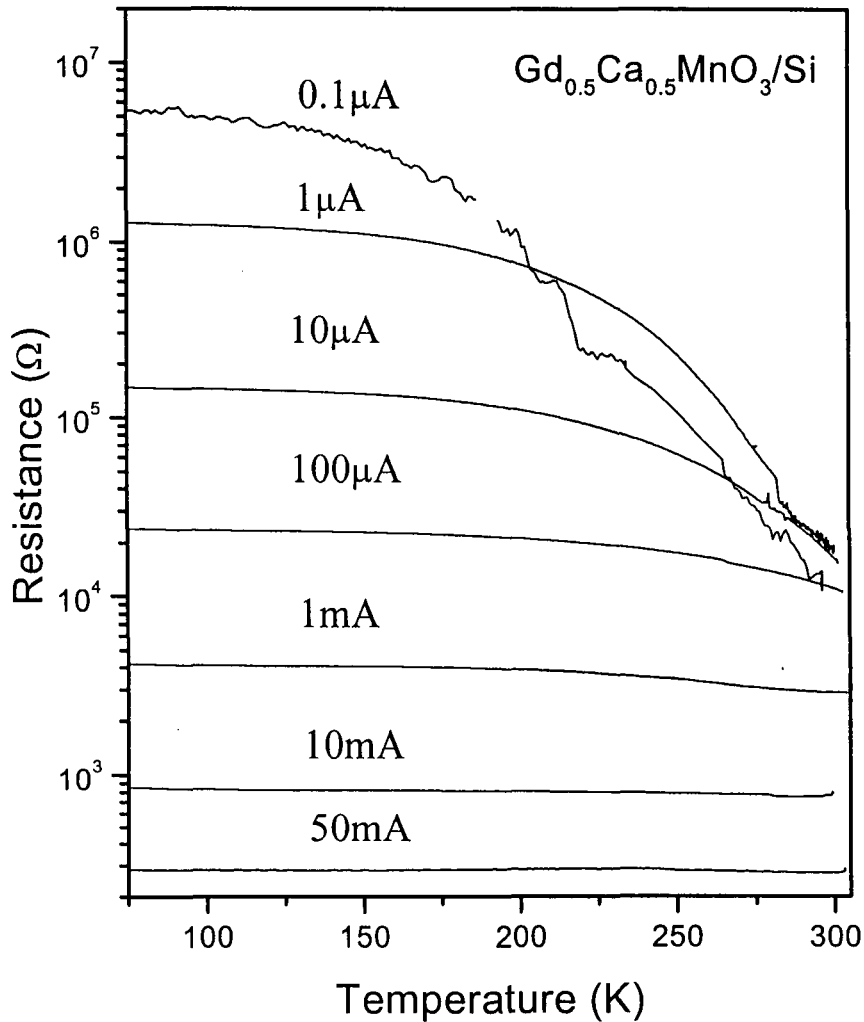


Fig.4.21 Temperature variation of the resistance of a polycrystalline $Gd_{0.5}Ca_{0.5}MnO_3$ film deposited on Si(100) for different current values

Trends similar to NCM on LAO(100) were found with the films of $Gd_{0.5}Ca_{0.5}MnO_3$ on LAO(100). Fig. 4.22 shows typical temperature dependence of resistance of a $Gd_{0.5}Ca_{0.5}MnO_3$ film deposited on LAO(100).

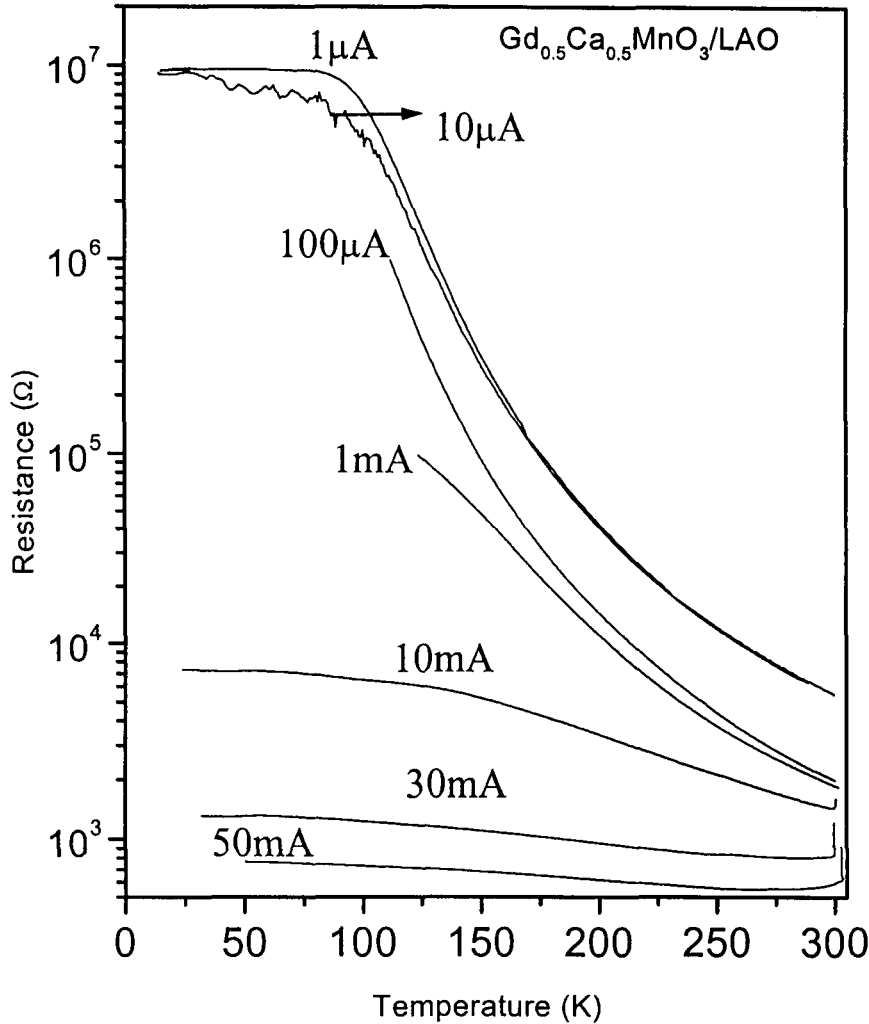


Fig.4. 22 Temperature variation of the resistance of an oriented $Gd_{0.5}Ca_{0.5}MnO_3$ film deposited on $LaAlO_3(100)$ for different values of current

In Fig. 4.23, we show the resistance vs temperature curves for a $Y_{0.5}Ca_{0.5}MnO_3$ film deposited on $Si(100)$, for different values of the current. We observe substantial decrease in resistnace with increase in current. The occurrence of a current-induced I-M transition in YCM is indeed noteworthy as the CO state in this material is very robust , being unaffected by magnetic fields or substitution of Mn^{3+} by Cr^{3+} and such ions. Trends similar to NCM and GCM on LAO(100) are found with the films of $Y_{0.5}Ca_{0.5}MnO_3$ on LAO(100). Fig.4.24 shows typical temperature dependence of resistance of a $Y_{0.5}Ca_{0.5}MnO_3$ film deposited on LAO(100).

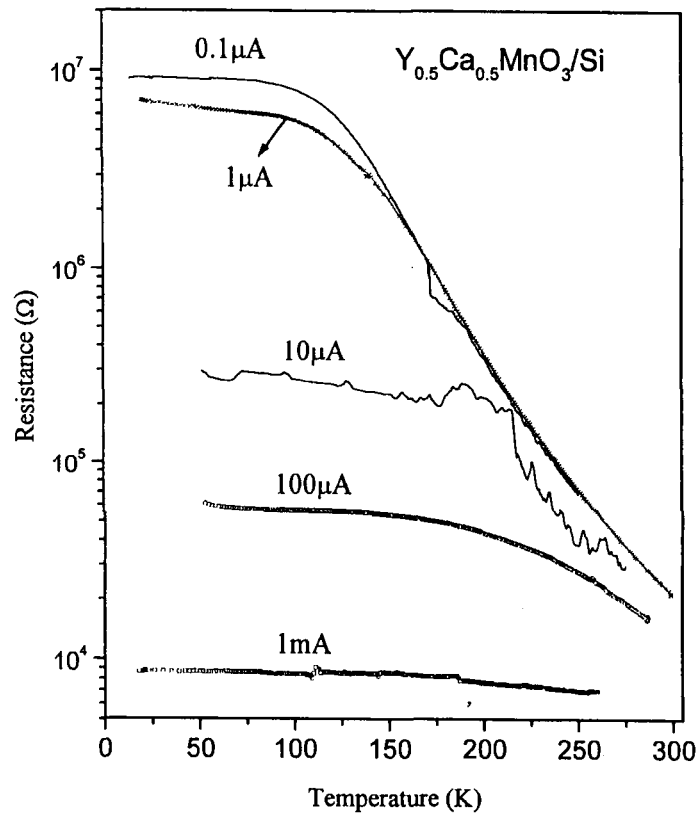


Fig.4.23 Temperature variation of the resistance of a polycrystalline $Y_{0.5}Ca_{0.5}MnO_3$ film for different current values

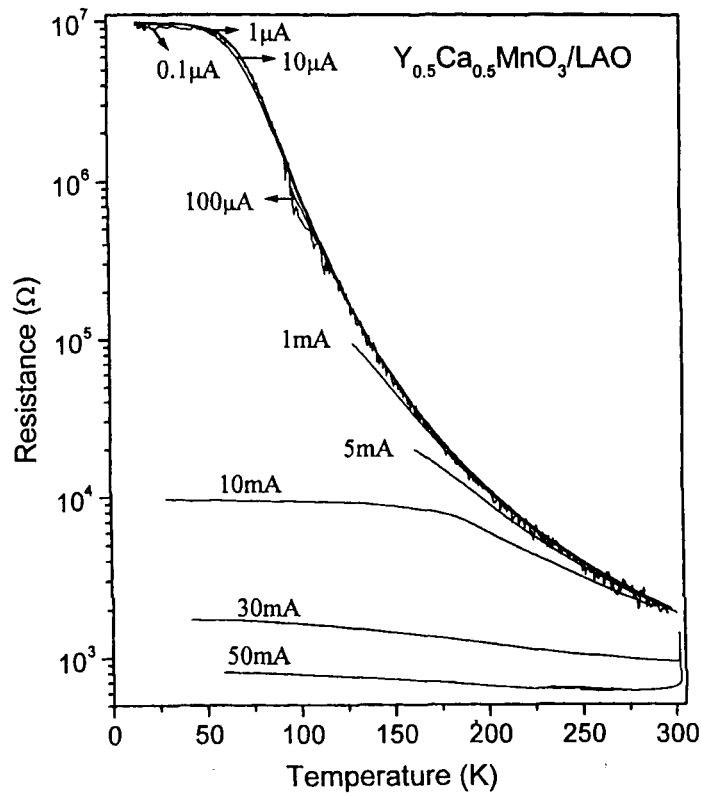


Fig.4.24 Temperature variation of the resistance of an oriented $Y_{0.5}Ca_{0.5}MnO_3$ film deposited on $LaAlO_3(100)$ for different values of current

(c) Current-Voltage (I-V) characteristics: A study of the I-V characteristics of the various manganese films reveals a non-ohmic behavior. Fig. 4.25 shows the I-V curves for NCM films deposited on Si(100) and LAO(100) substrates. On Si(100) substrate the non-ohmic behavior is seen only below 150K. But on the other hand the oriented films on LAO(100) show a non-ohmic behavior at ~250K. This is due to high resistance of the films on LAO(100) as compared to Si(100). Detailed theoretical investigations are under progress.

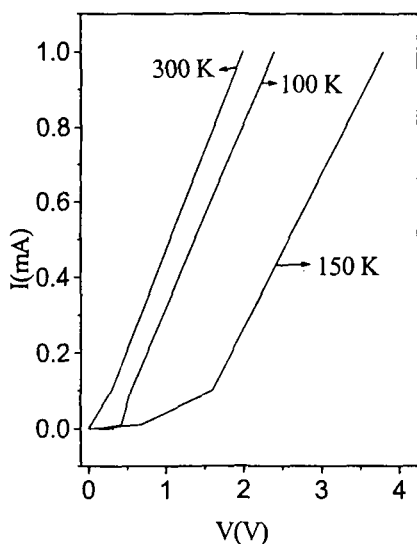


Fig.4.25a I-V characteristics of a $Nd_{0.5}Ca_{0.5}MnO_3$ film deposited on Si(100).

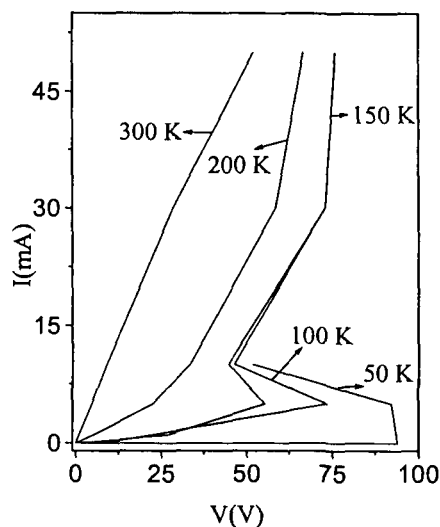


Fig.4.25b I-V characteristics of a $Nd_{0.5}Ca_{0.5}MnO_3$ film deposited on LAO(100).

Similar trends like those of NCM were observed with the GCM films. There also a clear non-ohmic behavior is seen in the films on both the substrates, but the negative differential resistance NDR and the switching to lower resistive states on LAO(100) is very sharp in this case as it is more robust charge ordered system than NCM. Fig.4.26 (a) and (b) show the I-V plot of the films of GCM on Si(100) and LAO(100) to illustrate the required behavior.

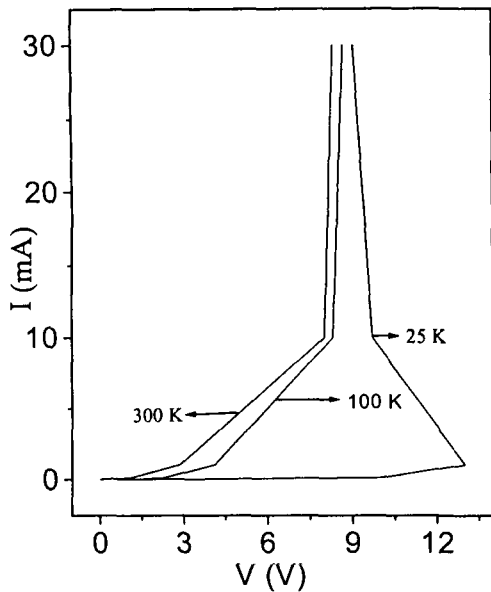


Fig.4.26a I-V characteristics of a $Gd_{0.5}Ca_{0.5}MnO_3$ film deposited on Si(100).

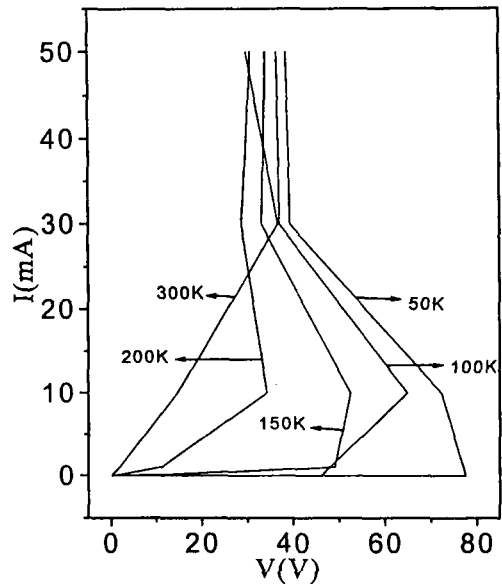


Fig.4.26b I-V characteristics of a $Gd_{0.5}Ca_{0.5}MnO_3$ film deposited on LAO(100).

YCM films exhibit I-V characteristics similar to those of NCM and GCM films. As this is the most robust of all the charge-ordered systems, the non-ohmic behavior is prominent even on the Si(100) substrate. Fig.4.27 (a) and (b) show I-V characteristics of the films of YCM on Si(100) and LAO(100).

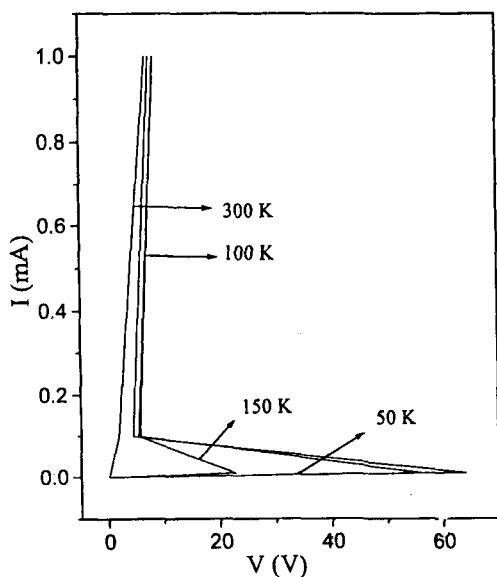


Fig.27a. I-V characteristics of a $Y_{0.5}Ca_{0.5}MnO_3$ film deposited on Si(100)

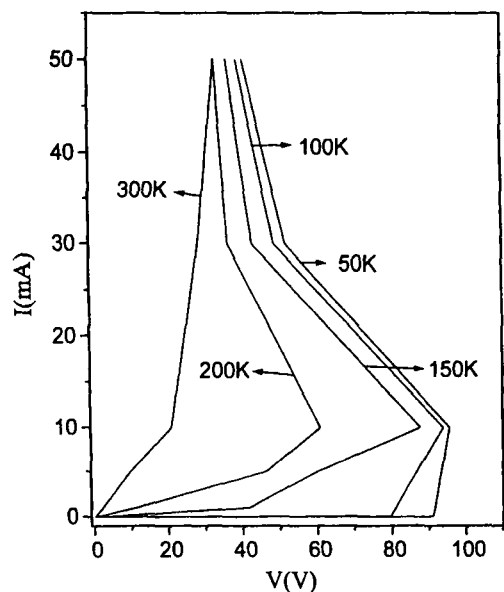


Fig.4.27b I-V characteristics of a $Y_{0.5}Ca_{0.5}MnO_3$ film deposited on LAO(100)

(d) **Switching phenomena:** The charge-ordered NCM, GCM and YCM films deposited on LAO(100) exhibit a huge memory effect. Fig.4.28 shows typical data on a film of NCM deposited on LAO(100). We see the occurrence of a hysteric I-M transition driven by transport current. The resistance-temperature plots (at constant transport current) are as described earlier when the sample is cooled from room temperature. After attaining the lowest temperature of measurement (~ 20 K), when the current is turned off, and on again, to carry out measurements as the films are heated, the heating curves show an abrupt drop

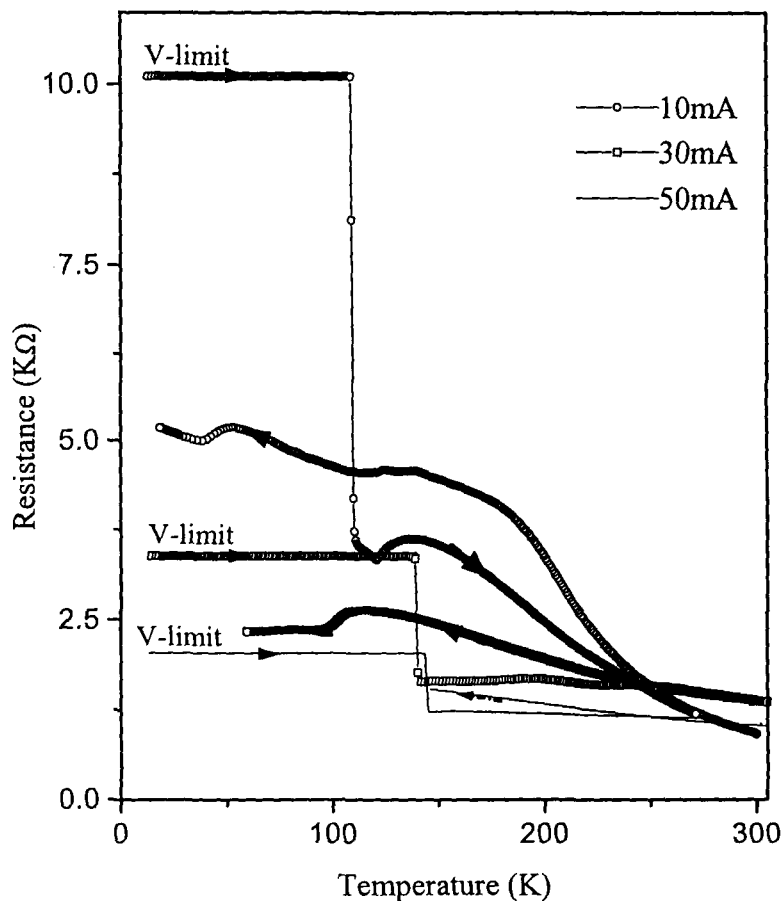


Fig. 4.28 Heating and cooling curves of d.c electrical transport of $Nd_{0.5}Ca_{0.5}MnO_3$ films on LAO(100)

around a temperature at which the charge solid apparently melts. The jump in resistance to the original value of the cooling curve (before the current was switched off) is indeed remarkable. Such a memory of resistance value registered in the CO state is a novel property. Similar observations were seen on the films of GCM and YCM on LAO(100) substrate with

rather greater memory effect than NCM films. Fig.4.29 and Fig.30 shows the memory effect on GCM and YCM on LAO(100).

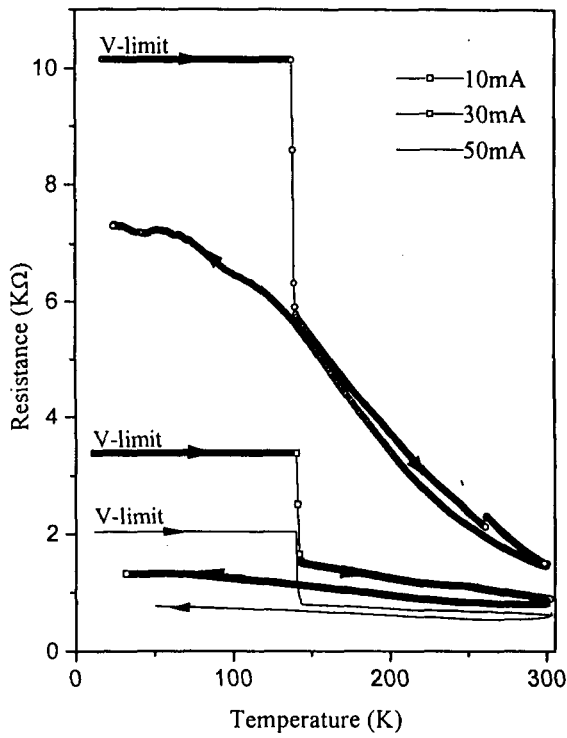


Fig. 4.29 Heating and cooling curves of d.c electrical transport on $Gd_{0.5}Ca_{0.5}MnO_3$ films on LAO(100)

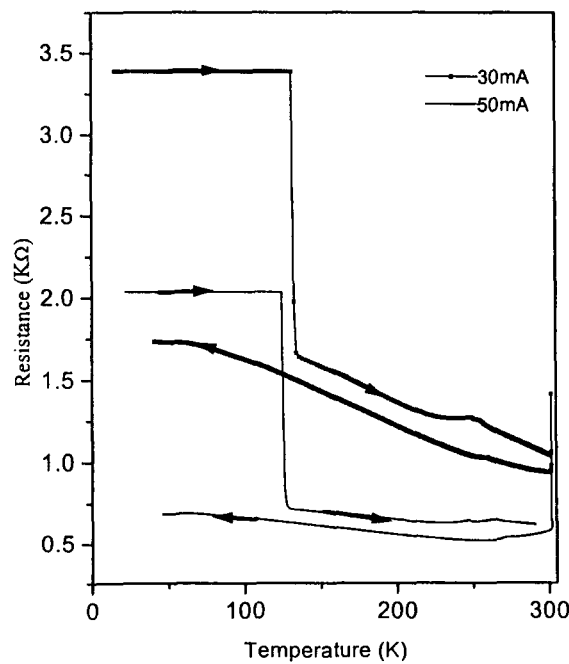


Fig. 4.30 Heating and cooling curves of d.c electrical transport of $Y_{0.5}Ca_{0.5}MnO_3$ films on LAO(100)

(e) **Study of $\text{Nd}_{0.5}\text{Sr}_{0.5}\text{MnO}_3$ films:** Figs.4.31a and b show the x-ray diffraction patterns of the films on Si(100) and LAO(100). The films have polycrystalline nature on Si(100) and are oriented in (100) direction on LAO(100). The films show a metallic behavior from ~ 300 K

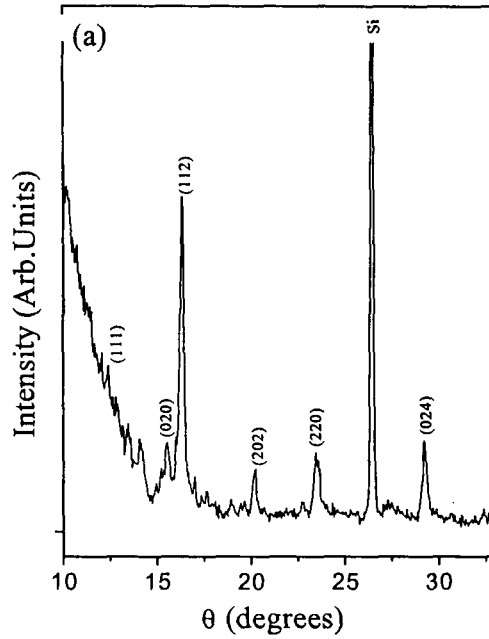


Fig.4.31a X-ray diffraction pattern of a polycrystalline $\text{Nd}_{0.5}\text{Sr}_{0.5}\text{MnO}_3$ film on Si(100)

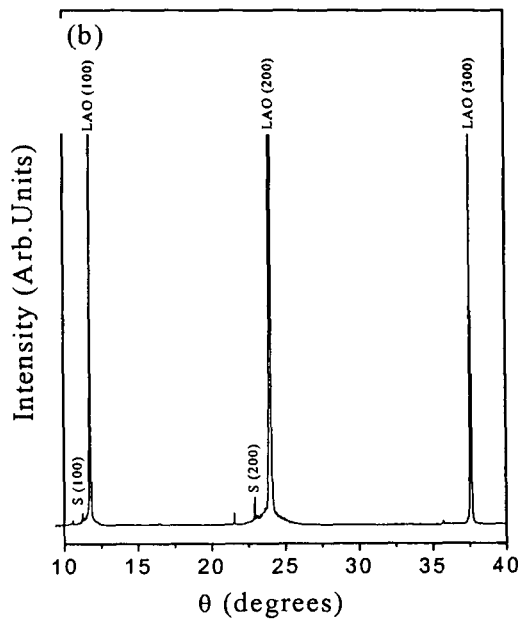


Fig.4.31b X-ray diffraction pattern of an oriented $\text{Nd}_{0.5}\text{Sr}_{0.5}\text{MnO}_3$ film on LAO(100) 'S' denotes film reflections due to the manganate.

down to ~ 140 K and resistance increases below 140 K due to charge-ordering. The increase in the CO state is not as sharp in the film as in a single crystal²⁵. We, however see that the high temperature metallic behavior occurs for all current values. The resistance decreases substantially in the charge-ordering regime, with increase in current. At 50mA, $\text{Nd}_{0.5}\text{Sr}_{0.5}\text{MnO}_3$ on $\text{Si}(100)$ (Fig.4.32) remains metallic from 300 K down to 20 K, although there is a slight heating of the sample at this current value. In the case of films on $\text{LAO}(100)$ (Fig.4.33), a behavior similar to that of NCM on $\text{LAO}(100)$ is observed.

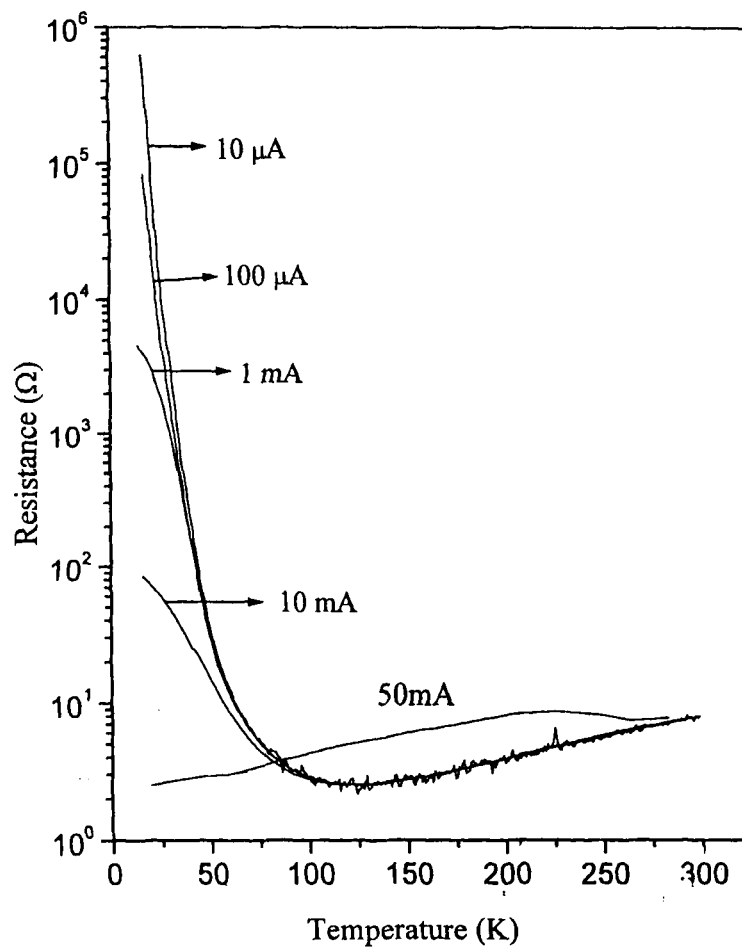


Fig.4.32 Temperature dependence of electrical resistance of a polycrystalline $\text{Nd}_{0.5}\text{Sr}_{0.5}\text{MnO}_3$ film on $\text{Si}(100)$

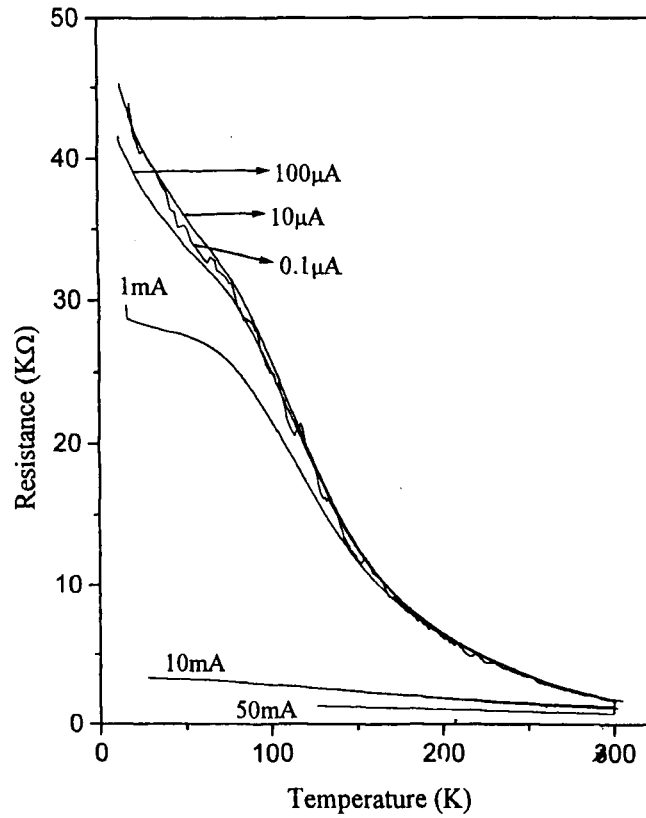


Fig.4.33 Temperature dependence of electrical resistance for an oriented film of $Nd_{0.5}Sr_{0.5}MnO_3$ on LAO(100)

As the NSM films show metallic behavior near room temperature, the I-V characteristics become non-ohmic only at very low temperatures on both the substrates. Figs.4.34a and b show the I-V characteristics of the NSM films on Si(100) and LAO(100).

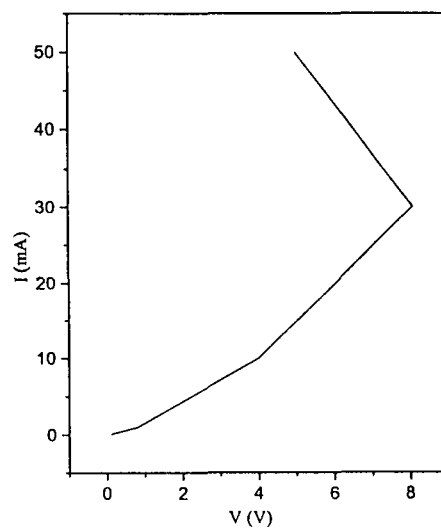


Fig.4.34a I-V characteristics of $Nd_{0.5}Sr_{0.5}MnO_3$ on Si(100)

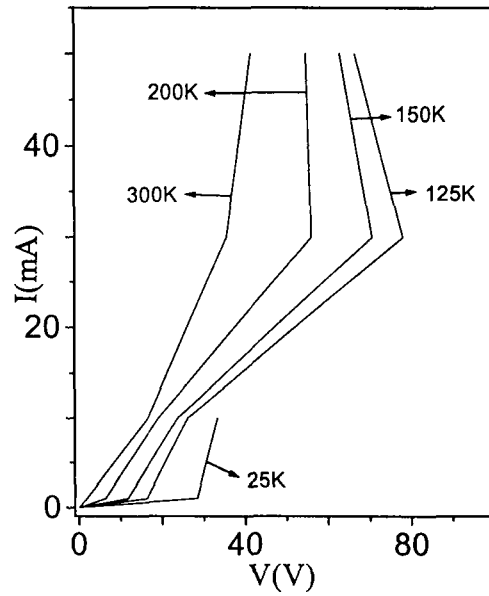


Fig.4.34b I-V characteristics of $\text{Nd}_{0.5}\text{Sr}_{0.5}\text{MnO}_3$ on $\text{LAO}(100)$

Similar to the NCM films, we could observe a switching behavior in the NSM films deposited on $\text{LAO}(100)$. Fig.4.35 shows the resistance behavior of a NSM film on $\text{LAO}(100)$ in cooling and heating cycles.

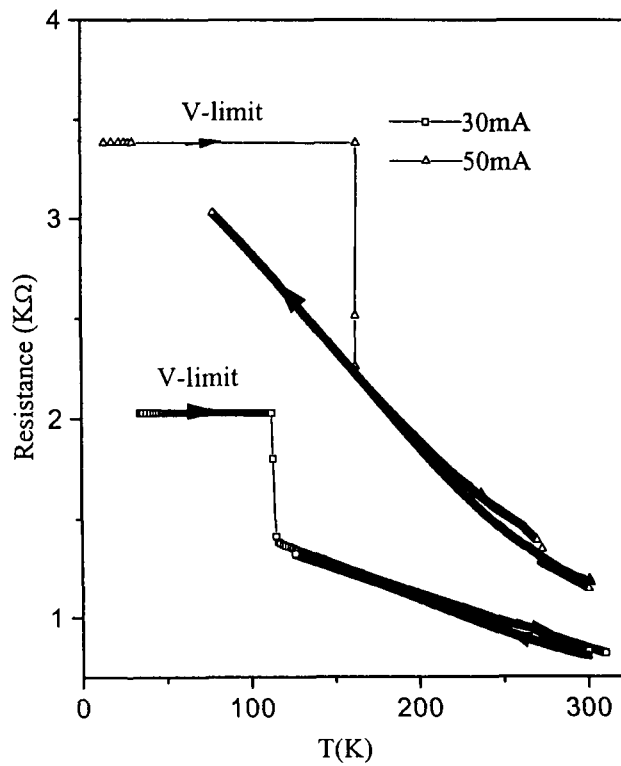


Fig.4.35 Heating and cooling curves of d.c. electrical transport of $\text{Nd}_{0.5}\text{Sr}_{0.5}\text{MnO}_3$ film on $\text{LAO}(100)$

(f) **Chemical doping of charge-ordered manganates:** The effect of cation substitution in the manganese site of charge-ordered rare earth manganates has been studied in bulk samples³¹. It has been found that the insulating CO state of $\text{Ln}_{0.5}\text{Ca}_{0.5}\text{MnO}_3$ ($\text{Ln} = \text{Nd, Gd}$ and Y) is unaffected by substitution with Al^{3+} and Fe^{3+} , but the CO state in $\text{Nd}_{0.5}\text{Ca}_{0.5}\text{MnO}_3$ ($\langle r_A \rangle = 1.17\text{\AA}$) is transformed into the ferromagnetic metallic state by Cr^{3+} substitution. Effects similar to the bulk have been found in the present study of NCM films. Thus, the

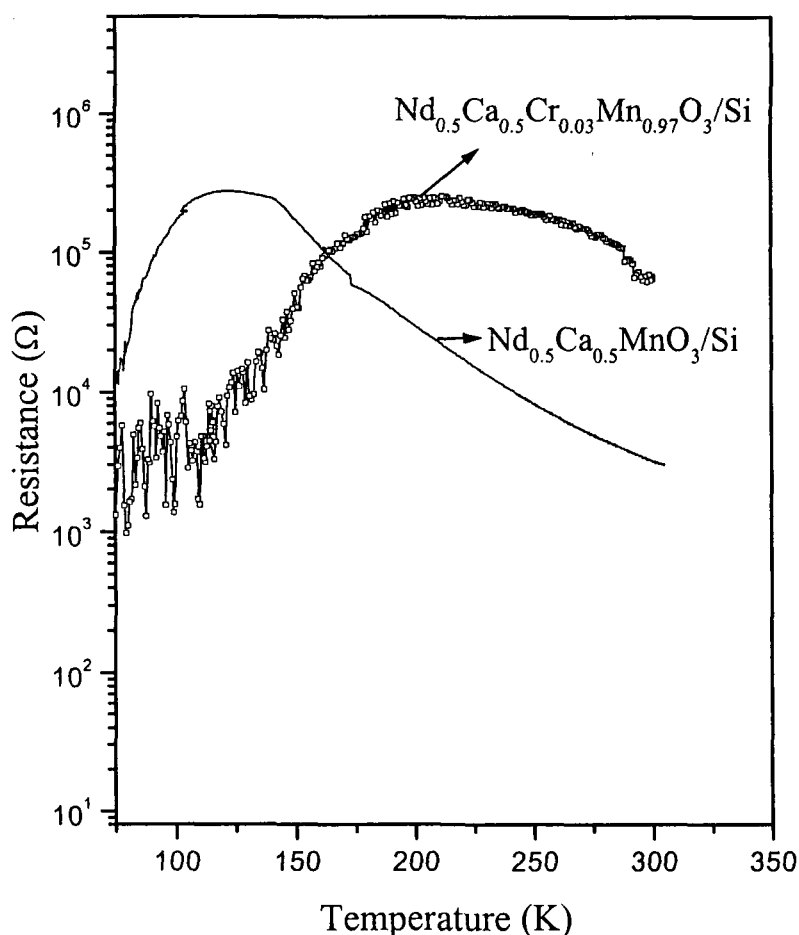


Fig.4.36 Comparison of temperature dependent d.c resistance of an undoped and doped film on Si(100)

NCM/Si(100) film exhibits melting of the charge-ordered state when doped with 3% Cr^{3+} . Fig.4.36 compares the resistance behavior of 3% Cr^{3+} doped film with that of the undoped film.

Chromium ion doped GCM films deposited on Si(100) show behavior different from the bulk. Fig.4.37 shows the temperature dependent resistance behavior of the Cr^{3+} doped and

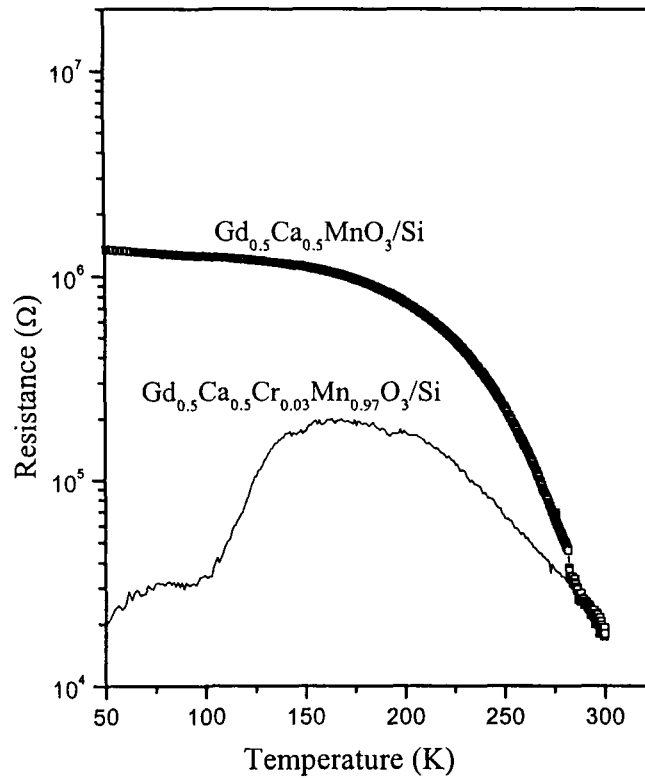


Fig.4.37 Comparison of temperature dependent d.c. resistance for undoped and Cr^{3+} doped GCM films on Si(100)

undoped films. The doped film shows evidence for melting, but this is not found in bulk samples. It is possible that part of the reason is the small differences in stoichiometry in the bulk and the films.

REFERENCES

1. Meissel L and Glang R 1970 Handbook of Thin Film Technology, Mc.Graw-Hill, New York.
2. Glocker David A and Shah S Ismat 1995 Handbook of Thin Film Technology, Institute of Physics Publishing.
3. Orlando Auciello and Jurgen Engemann 1993 NATO ASI SERIES E: Applied Sciences **234**.
4. Vossen John L and Kern Werner 1978 Thin Film Processes, Academic Press.
5. Ohring Milton 1992 Material Science of Thin Films Academic Press.
6. Raju A R, Aiyer H N and Rao C N R 1995 Chem. Mater. **7**, 225.
7. Aiyer H N, Raju A R and Rao C N R 1997 Chem. Mater. **9**, 755.
8. Langlet M and Joubert J C Chemistry of Advanced Materials, Edited Rao C N R, IUPAC 21st Century Monographs series, Blackwell Sci. Pub. Oxford, 1993, 55.
9. Mausbach M, Ehrich H and Muller K G 1991 Mat. Sci. and Engineering A **140**, 825.
10. Thomas P A, Brodsky M H, Kaplan D and Lepine D 1978 Phys. Rev. **B18**, 3059.
11. Yehoda J E , Yang B, Vedam K and Messier R J 1988 Vac. Sci. Technol. **A6**, 1631.
12. Reynolds S K, Smart C J, Baran E F , Baum T H, Carlson C E and Brock P J 1991 Appl. Phys. Lett. **59**, 2332.
13. Naik M B, Gill W N, Wentorf R H and Reeves R R 1995 Thin Solid Films **60**, 262.
14. Chiang C M, Miller T M and Dubois L H 1993 J. Phys. Chem. **97**, 11781.
15. Girolami G S, Jeffries P M and Dubois L H 1993 J. Am. Chem. Soc. **115**, 1015.
16. Li M, Wang G C and Min H G 1998 J. Appl. Phys. **83**, 5313.
17. Maruyama T 1997 Jpn. J. Appl. Phys. **36**, 6A, L705.

18. Childress J R and Chien C L 1991 Phys.Rev. **B4**, 8089.
19. Berkowitz A E, Mitchell J R, Carey M J, Young A P, Zang S, Spada F E,
Parker F T, Hutten A and Thomas G 1992 Phys. Rev. Lett. **68**, 3745.
20. Berkowitz A E, Mitchell J R, Carey M J, Rao A P, Rao D, Starr A, Zang S,
Spada F E, Parker F T, Hutten A and Thomas G 1994 J. Appl. Phys. **73**, 5320.
21. Wang W, Zhu F, Weng J, Xiao J and Lai W 1998 Appl. Phys. Lett. **72**, 1118.
22. Tokura Y 1998 Current Opinion in Solid State and Materials Science **4**, 175;
Tokura Y, Tomiyoka Y, Kuwahara H, Asamitsu A, Moritomo Y and Kasai M 1996
J. Appl. Phys. **79** 5288; Ramirez A P 1997 J. Phys. Condens. Matter **9**, 8171.
23. Rao C N R and Raveau B, Eds., Colossal magnetoresistance, Charge Ordering and
related properties of Manganese Oxides, World Scientific Pub., 1998; Rao C N R,
Arulraj A, Santhosh P N and Cheetham A K 1998 Chem.Mater. **10**, 2714.
24. Arulraj A, Santhosh P N, Gopalan R S, Guha A, Raychaudhuri A K, Kumar N and
Rao C N R 1998 J. Phys. Condens. Matter **10**, 8497.
25. Kuwahara H, Tomioka Y, Asamitsu A, Moritomo Y and Tokura Y, 1995 Science,
270, 961.
26. Asamitsu A, Tomioka Y, Kuwahara H and Tokura Y 1997 Nature **388**, 50.
27. Ogawa K, Wei W, Miyano K, Tomiyoka Y and Tokura Y 1998 Phys. Rev. **B57**,
R15033; Fiebig M, Miyano K, Tomiyoka Y and Tokura Y 1998 Science
280, 1925.
28. Xiong G C, Li Q, Ju H L, Green R L and Venkatesan T 1995, Appl. Phys. Lett. **66**,
1689.
29. Synder J G, Hiskes R, DiCarolis S, Beasley M R and Geballe T H 1996 Phys. Rev.
B53, 14434; Wang J Q, Barker R C, Cui G J, Tamagawa T and Halpern B L 1997
Appl. Phys. Lett. **71**, 3418.

30. Raju A R, Aiyer H N, Nagaraju B V, Mahendiren R, Raychaudhuri A K and Rao C N R 1997 *J. Phys. D: Appl. Phys.* **30**, L71.
31. Vanitha P V, Singh R S, Natarajan S and Rao C N R 1998 *J. Solid State Chem.* **10**, 2714
32. Langlet M, Labeau M, Bochu B and Joubert J C 1986 *IEEE Trans. Mag.* **22**, 151.
33. Labeau M, Reboux V, Dharhi D and Joubert J C 1986 *Thin solid films* **136**, 257.
34. Desisto W, Sosnowski M, Smith F, Deluca J, Kershaw R, Dwight K and Wold A 1989 *Mat. Res. Bull.* **24**, 753.
35. Qian Y T, Kershaw R, Dwight K and Wold A 1990 *Mat. Res. Bull.* **25**, 1243.
36. Xu W W, Kershaw R, Dwight K and Wold A 1990 *Mat. Res. Bull.* **25**, 1385
37. Haertling G H 1991 *J. Vac. Sci Tech.* **A9**, 414.
38. Ramaswamy G, Raychaudhuri A K, Goswami J and Shivashankar S A 1997 *J. Appl. Phys.* **82**, 3797.
39. Kim D J, Wentorf R H and Gill W N 1993 *J. Electrochem. Soc.* **140**, 3267.
40. Yoen H Y, Park Y B and Rhee S W 1997 *J. Mater. Sci.: Mater. in Electronics*
41. Pai P L and Ting C H 1989 *IEEE Elect. Dev. Lett.* **10**, 423.
42. Pai P L, Ting C H, Chiang C, Wei C S and Fraser D B 1990 *Proceedings of the 1989 Workshop, Materials Research Society, Pittsburgh (PA)* **359**.
43. Siegal R W 1960 *Philos. Mag.* **13**, 337.
44. Andrews P V, West M B and Robeson C B 1969 *Phil. Mag.* **19**, 887.
45. Chopra K L, Suri R and Thakur A P 1977 *J. Appl. Phys.* **48**, 538.
46. Rossiter P L and Bass J 1991 *Materials Science and Technology* eds. Cahn R W, Hansen P and Kramer E J (VCH Weinheim) **3A**, 257.
47. Mayadas A F and Shatzkes M 1970 *Phys. Rev.* **B1**, 1382.

48. Fuchs K 1938 Proc. Camb. Philos. Soc. 34, 100.

49. Sambles J R, Elsom K C and Jarvis D J 1982 Phil. Trans. R. Soc. London A304, 365.

530.417 S
N99

JNCASR

Acc
No. - 3020

LIBRARY